

Facile synthesis of direct Z-scheme PPy/NH₂-UiO-66 heterojunction for enhanced photocatalytic Cr(VI) reduction, industrial electroplating wastewater treatment, and tetracycline degradation

Qi Wang ^a, Shuzhen Zheng ^a, Wanggang Ma ^c, Jianying Qian ^d, Lingye Huang ^a, Hao Deng ^a, Qi Zhou ^a, Sirui Zheng ^a, Shuangjun Li ^e, Hao Du ^a, Qiang Li ^a, Derek Hao ^f, Guoxiang Yang ^{a,b,*}

^a School of Environmental Science and Engineering, Zhejiang Gongshang University, Hangzhou 310018, China

^b International Science and Technology Cooperation Platform for Low-Carbon Recycling of Waste and Green Development, Zhejiang Gongshang University, Hangzhou 310012, China

^c Hangzhou Hangda Environmental Protection Engineering Co., Ltd, Hangzhou 311222, China

^d CCTEG Hangzhou Research Institute Co., Ltd, Hangzhou 311200, China

^e The Education Ministry Key Lab of Resource Chemistry, Joint International Research Laboratory of Resource Chemistry of Ministry of Education, Shanghai Key Laboratory of Rare Earth Functional Materials, and Shanghai Frontiers Science Center of Biomimetic Catalysis, Shanghai Normal University, Shanghai 200234, China

^f School of Science, RMIT University, Melbourne 3000, Australia



ARTICLE INFO

Keywords:

NH₂-UiO-66

PPy

Z-scheme heterojunction

Photocatalysis

Cr(VI) reduction

ABSTRACT

Z-scheme heterojunction photocatalysts generally have excellent redox ability and robust removal efficiency for contaminants in water. Herein, we combined p-type PPy and n-type NH₂-UiO-66 by ball milling to prepare a direct Z-scheme PPy/NH₂-UiO-66 photocatalyst with ultra-high redox potential. Notably, the optimized efficiency of PPy/NH₂-UiO-66 (the mass ratio of PPy to NH₂-UiO-66 is 1 wt%, named PPy/NU-1) rapidly reduced Cr (VI) (>95%, 60 min) and TC degradation (>90%, 180 min) at 100 W LED light. Moreover, the PPy/NU-1 has high stability and good anti-interference ability, which can effectively remove Cr(VI) from industrial electroplating wastewater, and the Cr(VI) removal rate is 99%, which meets the industrial wastewater standard and has the potential attraction of actual wastewater treatment. In addition, the techniques of UV-Vis diffuse reflection, electron spin resonance (ESR), photoluminescence (PL), and photoelectrochemical measurement showed that PPy/NH₂-UiO-66 composites improved the light capture ability, thereby improving the photocatalytic efficiency. The PPy/NU-1 has a very high redox potential by constructing a Z-scheme heterojunction, enhances the interfacial charge transfer ability, and improves the separation efficiency of photogenerated carriers. Finally, the mechanism of the Z-scheme was systematically by nitroblue tetrazolium (NBT) and p-phthalic acid (TA) transformation, ESR experiments, and density functional theory (DFT) calculations. This work provides a strategy for the preparation of visible photocatalysts with excellent photocatalytic activity and provides new insights for interfacial charge transfer and molecular oxygen activation.

1. Introduction

In the past few decades, environmental ecosystem problems caused by environmental pollution have put tremendous pressure on the scientific community. Among them, wastewater treatment is considered to be one of the most challenging tasks. The main sources of water pollution are inorganic heavy metal ions and organic pollutants. Among heavy metal pollutants, chromium (VI) (Cr(VI)) is a common heavy metal pollutant in industrial wastewater of electroplating, leather

manufacturing, and pigment production [1]. Under different pH conditions, Cr(VI) showed three different oxyanions: Cr₂O₇²⁻, HCrO₄, and CrO₄²⁻ [2]. Due to the chemical stability and good water solubility of Cr (VI) oxyanions, they have the characteristics of high mobility. However, due to the toxicity, it poses a threat to the safety of drinking water sources and the health of the ecological environment. In addition, although antibiotics such as tetracycline (TC) play an indispensable role in human and veterinary medicines, they are often improperly treated after use, causing their residues to accumulate in the water environment,

* Corresponding author at: School of Environmental Science and Engineering, Zhejiang Gongshang University, Hangzhou 310018, China.

E-mail address: yangguoxiang@zjgsu.edu.cn (G. Yang).

which also threatens the ecological environment and human health [3, 4]. Therefore, it is important to find a cost-effective and efficient method to treat wastewater containing Cr(VI) and antibiotics.

At present, Cr(VI) treatment technology mainly includes adsorption, membrane separation, chemical reduction, and so on [5–7]. However, the above methods have problems, such as high operating costs and secondary pollution. For the removal of antibiotics from water bodies, traditional methods such as filtration, adsorption, and biodegradation are usually used. Unfortunately, antibiotics are difficult to effectively eliminate with conventional methods due to their high stability and resistance to biological treatments [8]. Therefore, there is an urgent need for an efficient, economical, and pollution-free environmental remediation method for the simultaneous removal of Cr(VI) and antibiotics.

In recent years, the photocatalytic reduction method has become one of the potential methods to solve the problem of Cr(VI) and antibiotic-containing wastewater due to its simple operation, recyclability, and no pollution [9]. Semiconductor photocatalysts are driven by solar energy to produce photogenerated electrons and reactive oxygen radicals at room temperature, reducing highly toxic Cr(VI) to low toxicity Cr(III), and then removing Cr(III) ions in alkaline aqueous solution by precipitation [10]. Antibiotic macromolecules are oxidized into low-toxicity small molecules and finally mineralized into inorganic carbon. Therefore, to promote the application of photocatalytic redox in wastewater, it is important to develop visible-light-driven photocatalysts with high activity, strong anti-interference ability, and high stability. In the early stage, inorganic semiconductors such as ZnO, BiOBr, and TiO₂ were mainly used for photocatalytic reduction of Cr(VI) and degradation of TC [11–13]. However, these inorganic semiconductors usually suffer from narrow light absorption and low photocatalytic efficiency. Therefore, it is of great significance to develop new photocatalysts for the reduction of Cr(VI) and degradation of antibiotics.

Recently, it has been found that synthesizing a direct Z-scheme heterojunction is sustainable in improving photocatalytic performance compared with the traditional modification strategy [14,15]. The direct Z-scheme heterojunction maintains the high redox property of photogenerated charge but also enhances the interfacial electron transfer ability, thus improving the photocatalytic activity. In addition, the catalytic performance of Z-scheme heterojunction reaction kinetics mainly depends on each single group of photocatalysts. Therefore, to maximize the high redox activity, the selection of constituent materials with a positive valence band (VB) potential and a negative conductivity band (CB) potential is one of the effective strategies. Li et al. reported that the design of direct Z-scheme heterojunction materials involved the regulation of an internal electric field (IEF), requiring the energy difference between component I's VB and component II's CB to be small [16].

At present, unlike traditional semiconductors, metal-organic frameworks (MOFs) are periodic crystal structures composed of organic ligands and self-assembly of metal ions [17]. Due to their unique structures and corresponding catalytic properties, they have attracted increasing attention worldwide. MOFs have the advantages of large specific surface area, adjustable structure, and photo-response of ligands, and can be directly used as photocatalysts or carriers-supported photocatalysts [18]. Among them, NH₂-UiO-66 (an n-type semiconductor) is a prospective photocatalyst thanks to its excellent stability and light responsiveness [19]. Because of amino functional groups (-NH₂), NH₂-UiO-66 can be excited by visible light. Moreover, under acidic conditions, -NH₂ can be protonated to form -NH₃⁺, which facilitates the adsorption of Cr(VI). In addition, the energy level structure of NH₂-UiO-66 satisfies the formation of •OH and •O₂. In summary, NH₂-UiO-66 has excellent performance due to its large specific surface area, adjustable active site, and robust stability. However, pure NH₂-UiO-66 exhibits rapid recombination of charge carriers, which limits its wide application. Fortunately, heterostructures can enhance charge separation.

In recent years, various conductive organic polymers (such as poly-pyrrole, polythiophene polyaniline, etc.) have been used to improve the performance of photocatalysts due to their unique π conjugation system, efficient electron transport capacity, high carrier mobility, and excellent optical properties [20]. Among them, the polypyrrole (PPy) is a P-type semiconductor with a wide range of visible light responses and has been proven to be an ideal additive to improve the photocatalytic performance of various semiconductors such as TiO₂, BiOBr, and CuWO₄ [21–23]. For instance, the g-C₃N₄ nanosheet [24], Ta₃N₅ [25], and TiO₂ [26] improved photocatalytic performance after composing with PPy. Liang et. al reported that photogenic holes of g-C₃N₄ could be transferred to PPy [27]. Ta₃N₅/PPy composite exhibited very high photocatalytic activity for overall water splitting [28]. These successful cases show that PPy improves the mobility of holes, induces the separation of electron-hole pairs, and thus enhances the photocatalytic activity. However, studies on photocatalytic reduction with a single PPy have rarely been reported. The weak oxidation capacity of PPy is due to its VB potential (~+1.5 V vs. NHE). A negative CB potential (~−2.0 V vs. NHE) indicates that it has strong reducibility [29]. This demonstrates the ability of PPy to easily generate abundant e[−] and •O₂ radicals, indicating its great potential for reducing. In addition, the VB potential of PPy is close to that of NH₂-UiO-66, which is consistent with the principle required to form a Z-scheme heterojunction. Therefore, we expect to design PPy/NH₂-UiO-66 with a high redox potential to further enhance the photocatalytic reduction of Cr(VI) performance.

Thus, in this paper, the ball milling strategy (Fig. 1) is used for the first time to disperse the polymer semiconductor PPy on the surface of NH₂-UiO-66 to form a direct Z-scheme heterojunction. Compared with the original NH₂-UiO-66, the energy band structure of the two compounds and the excellent conductivity of PPy make the composite material have stronger charge separation and visible light catalytic performance. The integration of NH₂-UiO-66 with PPy prevents PPy from agglomerating while improving light absorption capacity. The construction of Z-scheme heterojunction promotes photogenerated charge separation efficiency, thus significantly enhancing the photocatalytic performance. The morphology, structure, and photoelectrochemistry of PPy/NH₂-UiO-66 were characterized. At the same time, the conditions of photocatalytic reduction of Cr(VI) were optimized, including the mass ratio of PPy and NH₂-UiO-66, pH, co-existing cations, anions, and organic acids. Through the practical application in the treatment of industrial electroplating wastewater, the photocatalytic performance of Z-scheme PPy/NH₂-UiO-66 heterojunction was verified. Then, the cyclic stability of the optimized catalyst was tested. In addition, the photocatalytic degradation of TC by PPy/NH₂-UiO-66 and the toxicity analysis of intermediate products in the reaction path were studied in detail. Through various characterization, verification experiments, and density functional theory (DFT), the Z-scheme heterojunctions photocatalyst has been fully elucidated. Finally, the mechanism of photocatalytic reduction of Cr(VI) and degradation of TC by a new PPy/NH₂-UiO-66 system is described.

2. Materials and methods

2.1. Chemicals

The chemical reagents required for this study are displayed in Supporting Information (SI, Text S1).

2.2. Synthesis methods

2.2.1. Synthesis of NH₂-UiO-66(Zr)

The preparation method of NH₂-UiO-66 was reported by reference and optimized [30]. Specifically, weight NH₂-BDC (0.81 g, 4.5 mmol) in 40 mL N, N-dimethylformamide (DMF), then added ZrCl₄ (4.5 mmol), HAc (17 mL), mixed well ultrasound, and then transferred the reaction mixture to 100 mL of stainless-steel reactor with PTFE lining, heated the

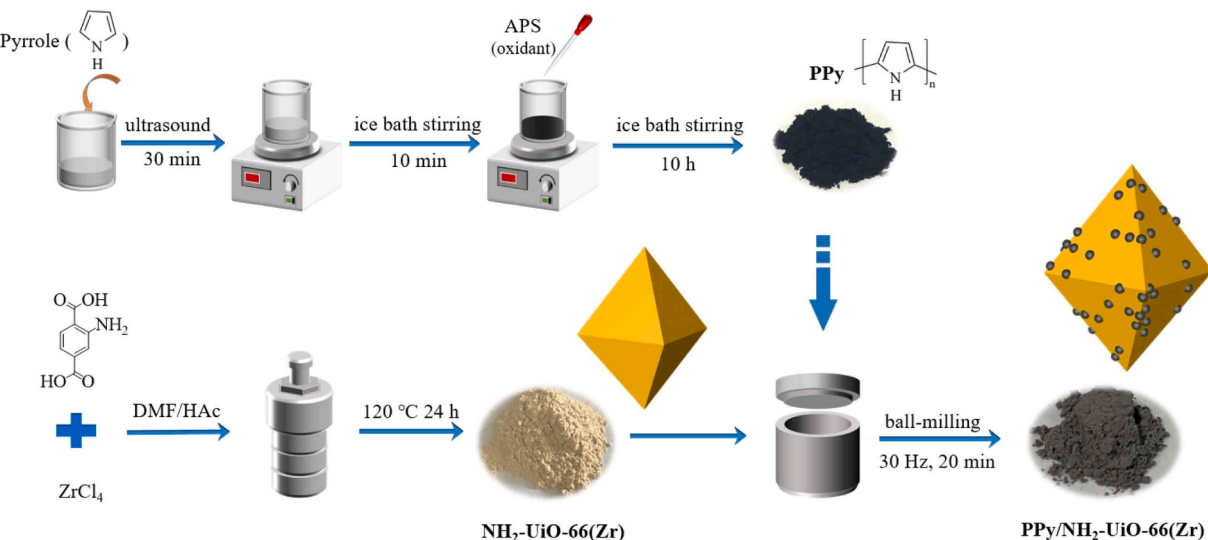


Fig. 1. Schematic representation of PPy/NU-66.

reaction at 120 °C for 24 h. After natural cooling to room temperature, centrifugal separation, finally, the solid products were washed with DMF and absolute ethanol 3 times and dried at 60 °C overnight before use. The resulting solids were labeled NU-66.

2.2.2. Synthesis of PPy

PPy was synthesized by reference using in situ polymerization [31]. The specific synthesis steps were as follows: add 1 mL of pyrrole to 50 mL of deionized water, sonicate for 30 min, stir in an ice water bath for 10 min, and wait for the solution to naturally drop to room temperature. 3.51 g of ammonium persulfate was dissolved in 20 mL of deionized water, and it was added to the above solution dropwise, after 10 h of ice water bath, it was washed 3 times with deionized water and absolute ethanol. The resulting black solid product was dried in a 60 °C oven for 12 h.

2.2.3. Synthesis of PPy/NH₂-UiO-66(Zr)

PPy/NH₂-UiO-66 composite preparation: the preparation process was shown in Fig. 1, prepared by ball milling, weighing a certain amount of PPy and NH₂-UiO-66(Zr) into the ball milling tank, loaded with 3 large balls and 4 small balls, the total quality control is 200 mg, and the ball milling at 30 Hz is 20 min, and the PPy load is 0.5–3 wt% PPy/NU-66 composite materials named PPy/NU (PPy/NU-0.5, PPy/NU-1, PPy/NU-2, PPy/NU-3). The physical mixture of PPy and NU-66 with the same content as PPy/NU-1 is recorded as PPy/NU-1 (PM).

2.3. Characterizations

The specific description is displayed in SI (Text S2).

2.4. Photoelectrochemical measurement

Details of the photoelectrochemical measurement are exhibited in SI (Text S3).

2.5. Evaluation of photocatalytic performance

Details are displayed in SI (Text S4).

2.6. Scavenging experiment and quantitative analysis of reactive oxide species (ROS)

Details are displayed in SI (Text S5).

2.7. Computational methods

Details are displayed in SI (Text S6).

3. Results and discussion

3.1. Morphological and structural characterizations

The morphology and microstructure characteristics of PPy, NU-66, and PPy/NU-1 were characterized by Scanning Electron Microscopy (SEM). Pure PPy presented a condensed nanosphere-spheroid-particle structure. The image showed the smooth surface of NU-66 with a triangular pyramidal (symmetrical crystal) topography and a size of around 2 μm [32]. PPy/NH₂-UiO-66(Zr) after ball milling was shown in Fig. 2, and the PPy particles were observed to be attached to the surface of NU-66, with mostly irregular octahedral morphology. At the same time, the element mapping showed that the composite contained C, N, O, and Zr. It can be further explained that PPy is dispersed on the surface of NU-66.

Transmission electron microscopy (TEM) further confirmed the presence of PPy nanoparticles. As shown in Fig. 3(a, b), PPy (gray) grew on the surface of NH₂-UiO-66 (black), indicating that PPy loading is on the surface of NH₂-UiO-66. Fig. 2c further clearly showed that PPy was interconnected with NH₂-UiO-66 and became irregular. TEM elemental line scan and EDX mapping analysis showed that PPy was uniformly distributed on the surface of NH₂-UiO-66 (Fig. 3(d-k)).

The composition and structural information of PPy, NU-66, and PPy/NU-1 composites were measured by XRD. As shown in Fig. 4, a broad peak appears at 20 = 24.6°, indicating that PPy is an amorphous organic polymer that is a repeat corresponding to a pyrrole ring unit [33]. The XRD spectra of PPy/NU-1 composites are similar to those of pure NU-66, indicating that PPy does not affect the crystal structure of NU-66. In particular, the 7.2°, 8.4°, and 25.7° positions correspond to the (111), (200), and (112) peaks of NH₂-UiO-66, respectively [34]. These results are consistent with data from the Cambridge Crystallographic Data Center (CCDC-1405751) [35]. On the contrary, no new peaks appeared, which indicates that the synthesis of NH₂-UiO-66/PPy compounds was perfect, but also that its structure was well preserved. Moreover, it was difficult to find obvious PPy diffraction peaks in PPy/NU-1 composites, which might be due to low PPy crystallinity and low PPy content.

FT-IR spectroscopy could be used to further determine the functional groups and chemical bonds. The FT-IR spectra of NU-66 showed Zr-O peaks at 600–800 cm⁻¹ (Fig. 4b) [30], the telescopic vibration peaks

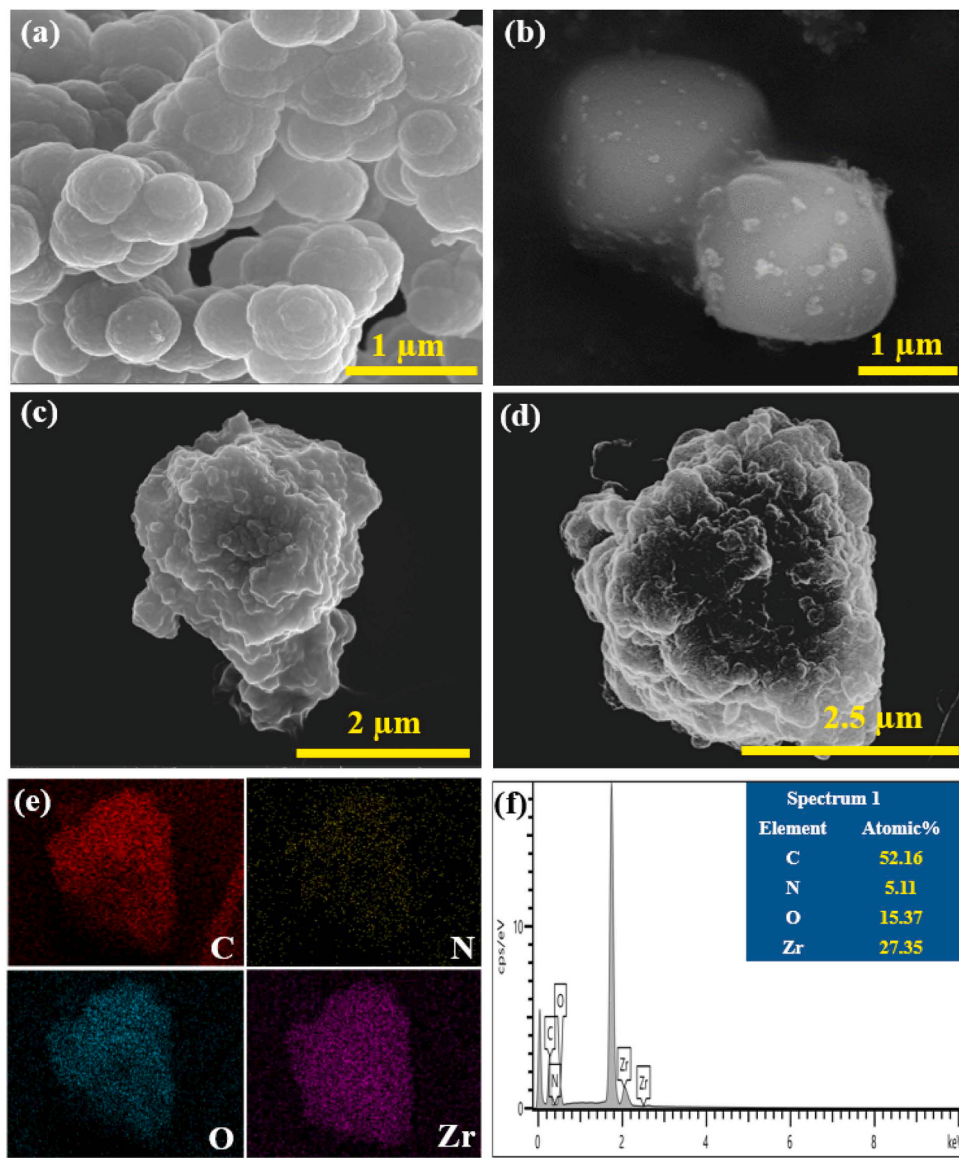


Fig. 2. SEM of (a) PPy, (b) NU-66, (c) PPy/NU-1, (d-e) EDS images of PPy/NU-1, (f) EDX of PPy/NU-1.

of $-\text{COOH}$ are distributed at 1578 cm^{-1} and 1385 cm^{-1} [30], and C-N, O-H, and C-H peaks appear at 1255 cm^{-1} , 765 cm^{-1} , and 664 cm^{-1} [36]. The characteristic peaks of PPy were located at 1536 cm^{-1} , 1286 cm^{-1} , 1164 cm^{-1} , and 1037 cm^{-1} , corresponding to the C-C tensile vibration, C-N tensile vibration, C-N in-plane deformation vibration and C-H in-plane vibration of the pyrrole ring [37–39], respectively, while the N-H peak was distributed in 770 cm^{-1} and 660 cm^{-1} [40]. The FT-IR spectra of PPy/NU-1 composites coincided with NU-66, and the presence of PPy characteristic peaks were also found, and the vibration peaks intensity at 1286 cm^{-1} , 1164 cm^{-1} , and 1037 cm^{-1} increased significantly, which confirmed the successful recombination of PPy and NU-66.

Fig. 4(c, d) shows the N_2 adsorption-desorption curve and pore size distribution of NU-66, PPy, and PPy/NU-1 composites. The BET of NU-66 and PPy were $877.0 \text{ m}^2 \text{ g}^{-1}$ and $11.4 \text{ m}^2 \text{ g}^{-1}$, respectively. After the introduction of PPy, the specific surface area of NU-66 decreased to $325.8 \text{ m}^2 \text{ g}^{-1}$. This was mainly because PPy entered the pores of $\text{NH}_2\text{-UiO-66}$, which reduced its pore volume from $0.41 \text{ cm}^3 \text{ g}^{-1}$ to $0.26 \text{ cm}^3 \text{ g}^{-1}$. NU-66 exhibits obvious I-type isotherm characteristics with a microporous structure [41]. PPy/NU-1 has a hysteresis loop, which is characterized by an H4-type hysteresis loop isotherm [42], with

microporous and mesoporous structures, and pore sizes of 0.56 nm and 2.7 nm . Compared with NU-66, the pore volume was reduced, indicating that ball milling did not destroy the structure of NU-66.

XPS characterization of NU-66, PPy, and PPy/NU-1 composites for further analysis of their constituent elements and chemical states. The total spectrum of XPS is shown in Fig. S1, and the components of PPy/NU-1 were detected as Zr, C, N, and O, which corresponded to the EDS test results. As shown in Fig. 5a, the C 1 s orbital of NU-66 is composed of $-\text{COOH}$, $\text{C}=\text{C}$, $\text{C}-\text{NH}_2$, and $\text{O}-\text{C}=\text{O}$, the binding energies of 284.6 eV , 285.0 eV , 285.7 eV and 288.8 eV [43], respectively, and C1s peak at 284.8 eV and 287.1 eV correspond to the $\text{C}=\text{C}/\text{C}-\text{C}$ and C-N of PPy [44], respectively. The N1s spectrum is shown in Fig. 5b, and PPy/NU-1 detected C-N and N-H bonds, with binding energies at 399.7 eV and 400.5 eV [45], respectively. As shown in Fig. 5c, the peaks at 531.1 eV and 531.9 eV in the O1s spectrum belong to the Zr-O and $-\text{COOH}$ bonds [46], respectively. Fig. 5d shows the Zr 3d spectrum, with peaks at 182.9 eV and 185.2 eV attributed to $\text{Zr } 3\text{d}_{5/2}$ and $\text{Zr } 3\text{d}_{3/2}$ [30], respectively. This further proved that PPy/NU-1 materials were successfully prepared. In addition, the binding energy of the C-N bond of the C1s peak in PPy/NU-1 was moving to 287.4 eV , while the binding energy of $\text{Zr } 3\text{d}_{5/2}$ and $\text{Zr } 3\text{d}_{3/2}$ in the Zr 3d peak is negatively shifted,

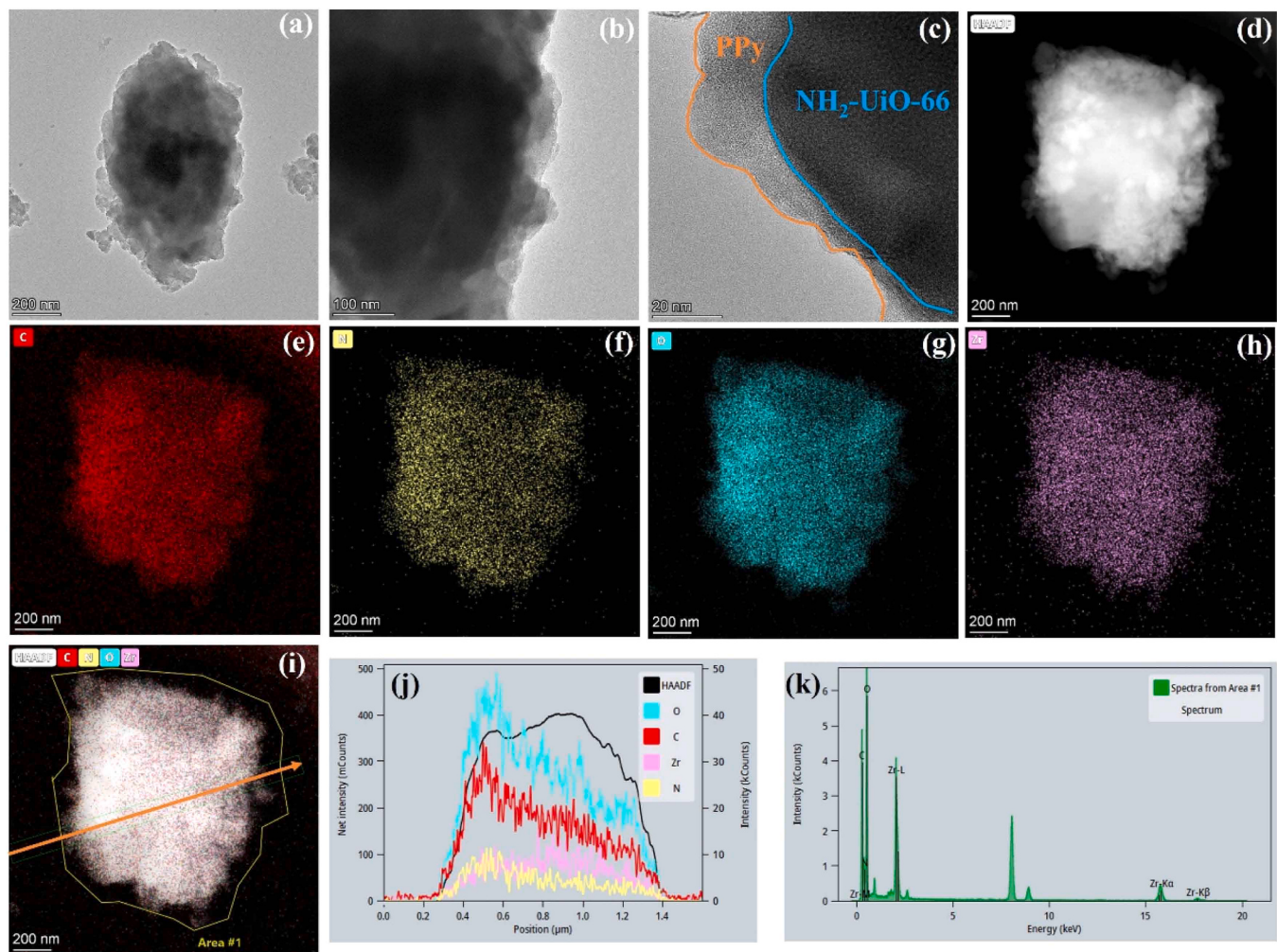


Fig. 3. (a, b) TEM of PPy/NU-1, (c) HRTEM of PPy/NU-1, (d) TEM EDS images of PPy/NU-1, the corresponding TEM elemental maps of (e) C, (f) N, (g) O, (h) Zr, (i, j) TEM elemental line scan across the PPy/NU-1, (f) TEM EDX of the PPy/NU-1.

which indicated that NU-66 interacts with PPy at the interface, and electrons transfer from PPy to NU-66.

3.2. Optical and photoelectrochemical properties

The optical properties of NU-66, PPy, and PPy/NU-1 materials can be analyzed using UV-Vis DRS, as shown in Fig. 6a. Pure NU-66 is buff and the color changes from buff to gray after the introduction of PPy. PPy black powder has strong light absorption in all bands (200–800 nm). The light absorption capacity of NU-66 and PPy/NU-1 composites was compared, and it was found that the light absorption capacity of PPy/NU-1 in the range of 440–800 nm was significantly improved. This is because the modification effect of PPy improves the utilization rate of light and the range of light absorption. According to the UV-vis DRS diagram, the corresponding band gap energy is calculated by the Kubelka-Munk equation: $\alpha h\nu = A(h\nu - Eg)^n$, where, A, Eg, v, h, and α respectively represent the constant, band gap, optical frequency, Planck constant and absorption coefficient. For the semiconductor material in this article, n is equal to 1/2 [47–49]. As shown in Fig. 6b, NU-66 and PPy are both direct bandgaps, and the bandgaps of NU-66, PPy, and PPy/NU-1 are calculated by formulating 2.91 eV, 2.31 eV, and 2.87 eV, respectively.

Fig. 7a shows the transient photocurrent patterns of NU-66, PPy, and PPy/NU-1, and when NU-66 is modified by the conductive polymer PPy, its photocurrent response is enhanced, which indicates that the introduction of PPy can significantly improve the carrier separation

efficiency. Fig. 7(b, c) is the EIS diagram of NU-66, PPy, and PPy/NU-1, the smaller the arc radius, the smaller the corresponding charge transfer resistance, the impedance ring radius in the dark state is greater than the impedance ring radius in visible light, and all follow the NU-66 > PPy/NU-1 > PPy order, indicating that the incorporation of PPy can significantly improve the conductivity of NU-66, promote the photogenerated electron-hole transport efficiency, and thus improve the visible photocatalytic performance. Fig. 7d shows PL spectra for different materials, all with an excitation wavelength of 350 nm. It can be seen that the PL strength of the PPy/NU composite is weaker than that of NU-66, indicating that Z-scheme can inhibit photogenerated charge recombination.

The Mott-Schottky curve can be used to determine the flat band potential (E_{fb}) and semiconductor type of PPy/NU-1. As shown in Fig. 7(e, f), NU-66 has a positive slope and PPy has a negative slope, indicating that NU-66 is an n-type semiconductor and PPy is a p-type semiconductor. The X-axis intercept of the curve shows that the E_{fb} values of NU-66 and PPy are -0.84 and 1.22 V vs. Ag/AgCl, equivalent to -0.64 , 1.42 V vs. NHE, respectively. However, the n-type semiconductor LUMO position will be minus 0.1 V higher than E_{fb} , and the p-type semiconductor HUMO position will be 0.1 V higher than E_{fb} , and the LUMO value of NU-66 can be calculated to be -0.74 V vs. NHE. PPy has a HUMO value of 1.52 V. From the UV-VIS DRS results, the Eg of NU-66 and PPy were determined to be 2.91 and 2.31 eV, respectively. Finally, according to the $E_{HUMO} = Eg + E_{LUMO}$ formula, the HUMO value of NU-66 is calculated as 2.17 V vs. NHE. PPy has a LUMO value of -0.79 V vs. NHE.

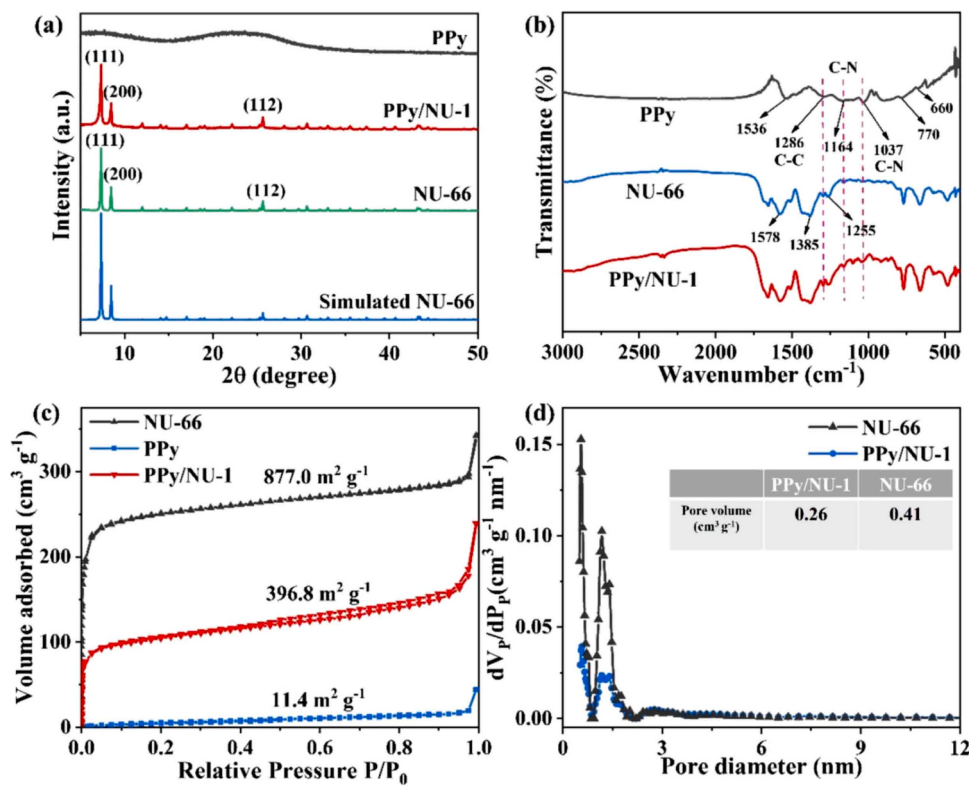


Fig. 4. (a) XRD patterns, (b) FTIR spectra, (c) N₂ adsorption-desorption, (d) BJH plots and pore volumes of NU-66 and PPy/NU-1.

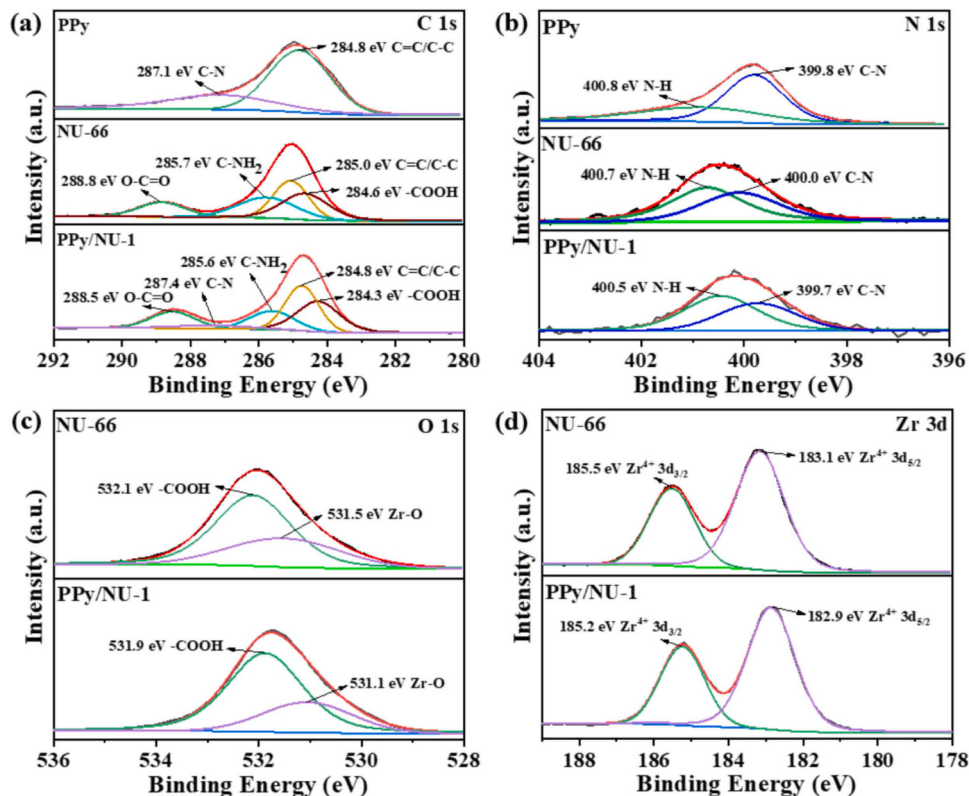


Fig. 5. Narrow XPS of PPy, NU-66, and PPy/NU-1: (a) C 1s, (b) N 1s, (c) O 1s, (d) Zr 3d.

3.3. Evaluation of photocatalytic reduction of Cr(VI) performance

To evaluate the photocatalytic activity of NU-66, PPy, and PPy/NU-1

materials, the heavy metal Cr(VI) was selected as the contaminant. The photoreduction kinetics of Cr(VI) (Fig. 8a), which was secretly adsorbed for 30 min before photoreaction to exclude the influence of adsorption

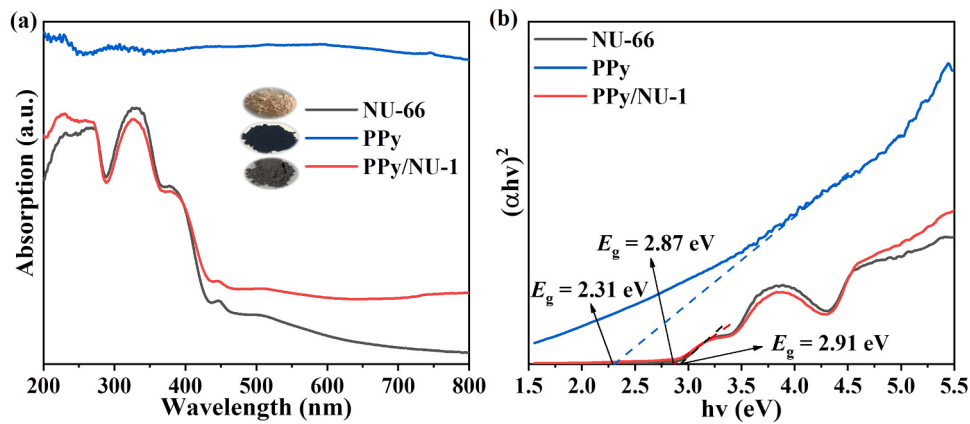


Fig. 6. (a) UV-vis DRS spectra and (b) Tauc plots of NU-66, PPy, and PPy/NU-1.

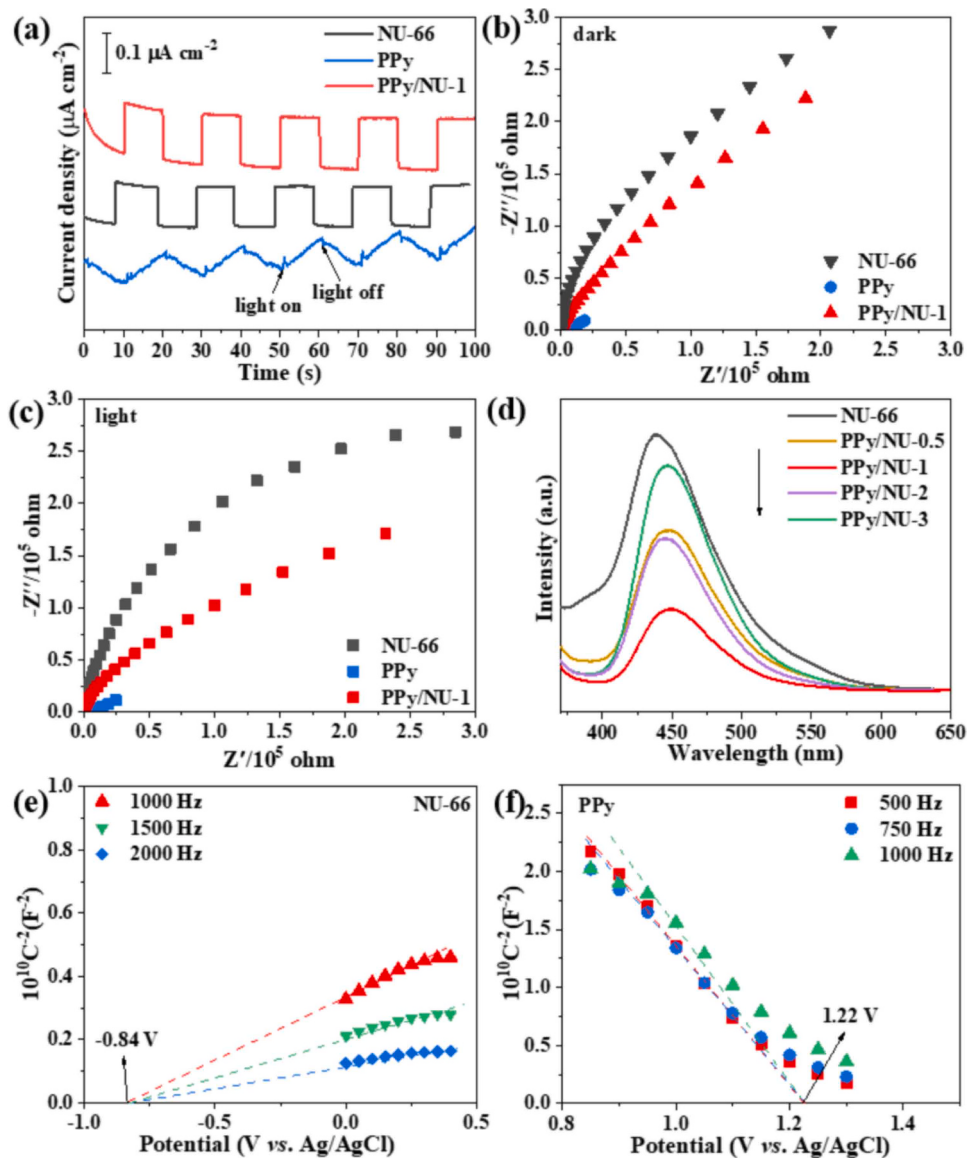


Fig. 7. (a) Transient photocurrent responses, (b) Nyquist plots in the dark, (c) and visible light, (d) PL spectra of NU-66, PPy, and PPy/NU-1, Mott-Schottky plots of (e) NU-66, (f) PPy.

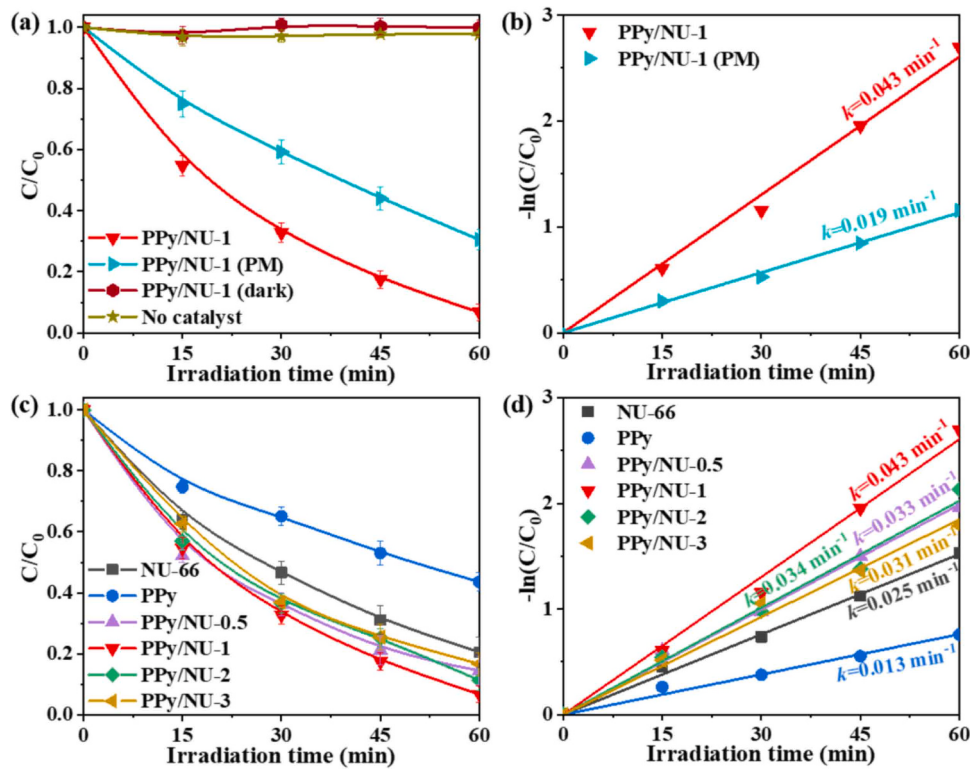


Fig. 8. (a-b) Photocatalytic Cr(VI) reduction and first-order rate constants, (c-d) and a series of PPy/NU.

on photoactivity. The photo-reducing Cr(VI) activity of all PPy/NH₂-UiO-66 was better than that of pure NH₂-UiO-66 and PPy, among which PPy/NU-1 had the highest photocatalytic activity, and the reduction rate was as high as 95% at 60 min, and the reaction rate constant was

0.043 min^{-1} , which was 1.72 and 3.31 times that of NU-66 and PPy, respectively (Fig. 8(c, b)). In addition, some controlled experiments have been done, such as without a catalyst or lack of light, there is almost no ability to reduce Cr(VI). The performance difference between

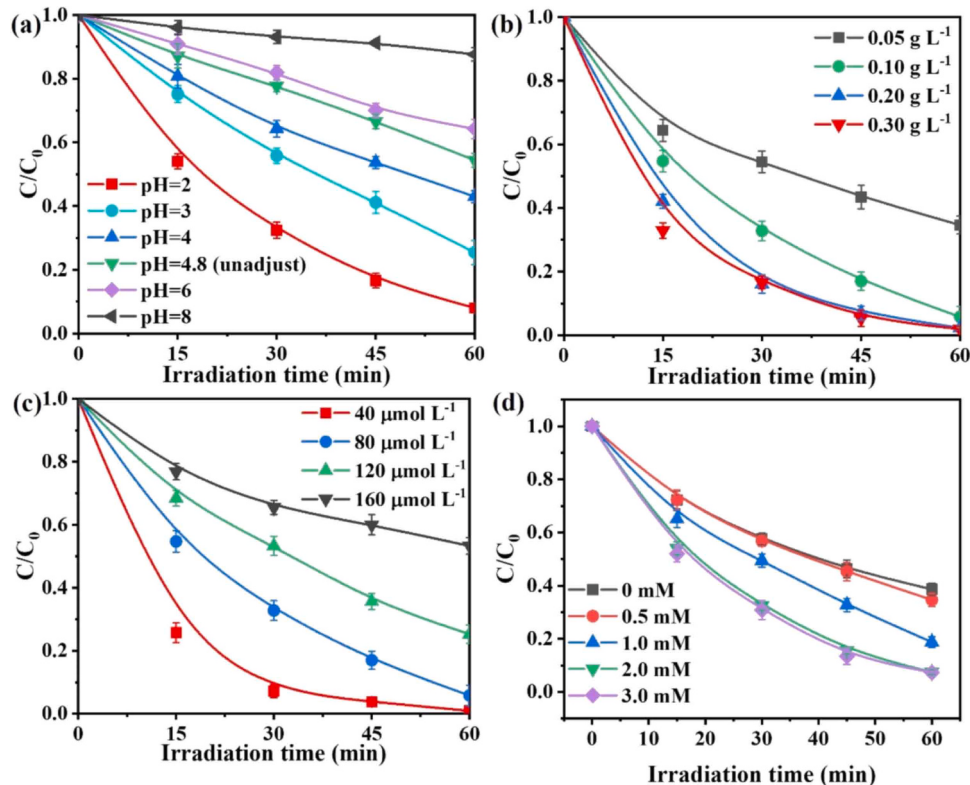


Fig. 9. The effects of (a) pH, (b) catalyst dosage, (c) initial Cr(VI), and (d) EDTA-2Na concentration.

PPy/NU-1 prepared by ball milling and mechanically mixed PPy/NU-1 (denoted as PPy/NU-1(PM)) was also compared, and the reduction rate of PPy/NU-1(PM) was only 68.5%, indicating the importance of constructing Z-scheme heterojunctions (Fig. 8b). Therefore, we selected PPy/NU-1 as the best photocatalyst for further research.

To obtain the most suitable reduction parameters, it is necessary to optimize the conditions of the solution in the process of PPy/NU-1 photocatalytic reduction of Cr⁶⁺. Because the pH value of Cr(VI)-containing wastewater is usually between 3 and 7, and the acidic conditions are conducive to the reduction of Cr(VI), the acidic conditions are mainly selected as the experimental parameters [50]. Fig. 9a shows the kinetic curve of the influence of the initial pH value of the solution on the photoreduction of Cr⁶⁺ by PPy/NU-1, and it is found that the reduction rate of Cr⁶⁺ decreases with the increase of pH, and the optimal pH is 2. The effects of PPy/NU-1 activity and different pH on the adsorption performance of Cr(VI) were explored, and the adsorption performance of PPy/NU-1 was found to have little change in the adsorption of Cr(VI) under different pH adsorption (Fig. S2). These results indicated that the improvement of the catalytic performance of PPy/NU-1 in reducing Cr(VI) at different pH was mainly due to photocatalysis. The reason is that the existence state of Cr⁶⁺ under different pH conditions is also different, Cr₂O₇²⁻ or HCrO₄ is mostly present in acidic environments, while CrO₄²⁻ is mostly present in alkaline conditions. The lower the pH, the higher the concentration of H⁺ in the environment, and the easier it is for Cr(VI) to be converted to Cr(III) [51, 52]; Conversely, the higher the pH, the easier it is for Cr(VI) to generate Cr(OH)₃ precipitate, which attaches to the surface of the catalyst and leads to a decrease in the active site and reduced activity. We tested that the pH of the solution after photocatalytic reduction was 2.5, indicating that after reduction, it mainly existed in the form of Cr(III), while the pH of PPy/NU-1 in water was 6.5, which was electrostatic repulsion of Cr (III) and would not be adsorbed on the catalyst, it was conducive to improving the cycling stability of the catalyst. The amount of catalyst was also optimized, and the results are shown in Fig. 9b. The amount of catalyst used was proportional to the catalytic activity, and when the dosage increased to 0.30 g L⁻¹, the performance hardly changed significantly. As shown in Fig. 9c, the higher the concentration of Cr⁶⁺ of the pollutant, the weaker the photoreduction performance of PPy/NU-1. Finally, the effect of the concentration of hole trap EDTA-2Na was also studied, as shown in Fig. 9d. Under illumination, the photogenerated holes on the catalyst will inhibit the reduction reaction, and the optimal EDTA-2Na concentration is 2.0 mM, at which time the holes in the solution have been completely quenched and the reduction rate is the highest, while further increasing the EDTA-2Na concentration has no obvious change in the reduction reaction. These results indicate that the reduction rate of Cr(VI) increases gradually with the increase of EDTA-2Na concentration in a certain EDTA-2Na concentration range. This promoting effect may be attributed to the presence of EDTA-2Na as a hole-scavenging agent. On the one hand, once the photogenerated hole (h⁺) is captured by the hole scavenger, the recombination of e⁻-h⁺ pairs will be inhibited, and more separated e⁻ in the conduction band can be transferred to the Cr(VI) reduction. On the other hand, the reduced Cr (III) may be oxidized back to Cr(VI) if the photogenerated h⁺ is not removed in time, and the addition of a hole scavenger (EDTA-2Na) will eliminate this interference [2, 53, 54].

In addition, the coexisting species may have a great impact on the performance of the photocatalytic Cr(VI) of PPy/NU-1 materials. Therefore, we comprehensively investigated the effects of different anions, cations, and organic acids (I⁻, Cl⁻, SO₄²⁻, NO₃⁻, CH₃COO⁻, Na⁺, Cu²⁺, Ba²⁺, Benzoic acid, Citric acid) on the removal of Cr(VI) [55–57]. By comparing the photocatalytic reduction performance of Cr(VI) under the coexistence of other ions or organic compounds at the same concentration, it was found that common cations, anions, and organic acids had almost no interference with the photocatalytic reduction effect of Cr(VI) (Fig. S3), indicating that PPy/NU-1 nanomaterials have good application potential for photocatalytic reduction of Cr(VI) in polyionic water.

Due to the different light absorption and utilization capacities of photocatalysts, the wavelength of incident light has different effects on the photocatalytic performance [55]. To this end, photocatalytic reduction of Cr(VI) experiments was carried out on PPy/NU-1 under different monochromatic light irradiation. As shown in Fig. S4, PPy/NU-1 exhibited excellent photocatalytic reduction performance of Cr(VI) under 380 nm and 450 nm light irradiation, and the photocatalytic performance gradually decreased with the increase of light wavelength, and its photo-absorption performance was mainly concentrated before 500 nm.

To further demonstrate the practical application of PPy/NU-1 in the removal of Cr(VI) in actual electroplating industrial wastewater, we configure the actual electroplating wastewater according to the main indicators of the reference literature to study the practical application value of the material [56, 57]. The main indexes of simulated electroplating wastewater are shown in Table S1. Fig. 10a shows that 100 mg of catalyst can remove more than 90% of Cr(VI) from simulated actual plating wastewater in 150 min under visible light irradiation. Interestingly, we treated the raw water samples of electroplating wastewater from Wenzhou Ouhuan Testing Technology Co., Ltd. and found that the removal rate of Cr(VI) reached more than 99% within 90 min of illumination (Fig. 10b). The above results show that PPy/NU-1 has a good application prospect in actual electroplating wastewater.

To study the reusability and stability of PPy/NU-1 Z-scheme heterojunction photocatalysts [58], five cycle experiments of Cr(VI) reduction were performed, and the results are shown in Fig. 11a. The photocatalytic activity of PPy/NU-1 is not significantly lost, and its photocatalytic efficiency can still be maintained well even after 5 runs. In addition, as shown in Fig. 11(b-d), the XRD pattern of PPy/NU-1 before and after cycling showed no significant differences in crystal structure and chemical bonds, and the specific surface area decreased slightly due to product clogging pore size. Combined with the above photocatalytic reduction experiments, the results show that PPy/NU-1 not only has excellent photocatalytic activity but also has excellent stability and reusability.

3.4. Evaluation of photocatalytic oxidative degradation of tetracycline (TC) performance

To evaluate the photocatalytic performance of PPy/NU-1 and its related samples, a tetracycline (TC) degradation test was carried out [59, 60]. As shown in Fig. 12a, the TC removal capacity of the prepared PPy/NU-1 composites is significantly enhanced, while the TC removal efficiency of NH₂-UiO-66 and PPy is very low. At the same time, as can be seen from Fig. 12b, the reaction rate constant k of PPy/NU-1 reaches 0.011 min⁻¹, which is 11 and 22 times higher than that of NH₂-UiO-66 (0.001 min⁻¹) and PPy (0.0005 min⁻¹), respectively.

To further study the active substances of PPy/NU-1 photocatalytic degradation of TC, we conducted free radical trapping experiments. Isopropanol (IPA), ascorbic acid (ASC), silver nitrate (AgNO₃), and ethylenediaminetetraacetic acid disodium salt (EDTA-2Na) were used to capture •OH, •O₂⁻, e⁻, and h⁺ radicals, respectively [61, 62]. As shown in Fig. 12c, the addition of AgNO₃ has no inhibitory effect on the reaction process, indicating that e⁻ is not an active substance in the reaction process. However, the degradation rates of TC were 33.0%, 36.9%, and 69.2%, respectively, which were 54.5%, 51.2%, and 18.66% lower than those without the addition of traps, indicating that the active substances involved in the photocatalytic reaction system were •O₂, h⁺ and •OH, while •O₂⁻ and h⁺ radicals were the main groups.

To better understand the TC degradation process induced by PPy/NU-1 heterojunction, the intermediates generated in the photocatalytic reaction were detected by the HPLC-MS system. According to previous studies, electron-donor groups and ionizable groups (e.g., dimethylamine, amide, double bonds) are susceptible to attack by reactive free radicals, resulting in TC decomposition [60, 63, 64]. To this end, in this work, two main TC degradation pathways on PPy/NU-1

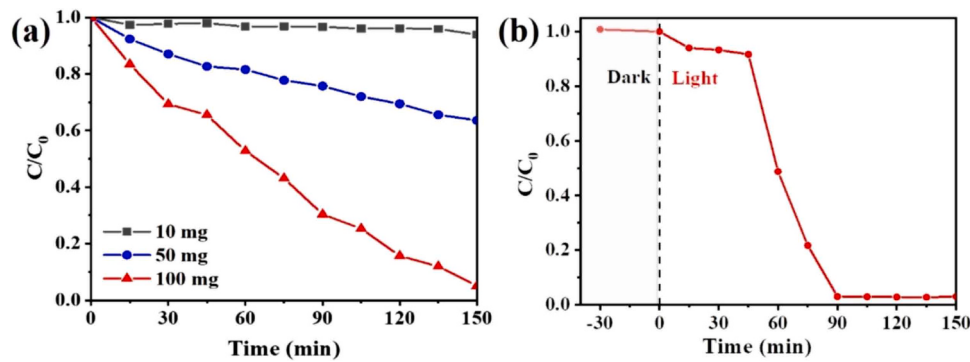


Fig. 10. (a) PPy/NU-1 pairs of different masses simulated the removal of Cr(VI) from actual electroplating wastewater (PPy/NU-1 and 100 mL of simulated electroplating wastewater with EDTA-2Na). (b) Cr(VI) removal from electroplating wastewater by PPy/NU-1 (100 mg catalyst and 100 mL of electroplating wastewater with 20 mmol/L EDTA-2Na).

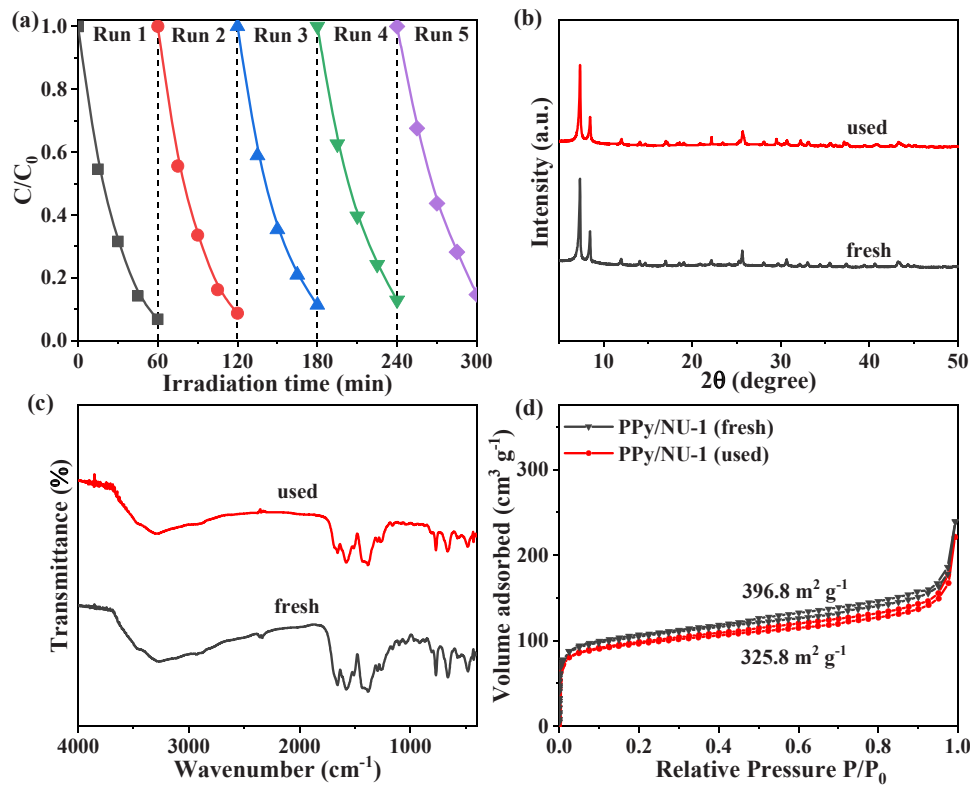


Fig. 11. (a) Recycling tests of PPy/NU-1. (b) XRD, (d) FT-IR, and (e) N₂ absorption-desorption of fresh and used PPy/NU-1.

were proposed, as shown in Fig. 12g. In pathway I, the amino group was easily attacked by $\bullet\text{O}_2^-$ and h^+ , and P1 ($m/z = 429$) was formed by deamination. P2 ($m/z = 413$) was formed by dehydroxylation, P3 ($m/z = 370$) was formed by demethylation and loss of methylamine groups P2 ($m/z = 413$), and P3 was further converted to P4 ($m/z = 346$) by a ring-opening reaction induced by $\bullet\text{O}_2^-$ and h^+ . P4 was then further degraded, and P5 ($m/z = 302$) was generated by continuous oxidation of $\bullet\text{O}_2^-$ and $\bullet\text{OH}$, which was consistent with previous observations. For pathway II, P6 ($m/z = 415$) was formed due to the loss of two methyl groups on saturated N atoms due to the attack of $\bullet\text{O}_2^-$. Subsequently, the conversion of P6 to P7 ($m/z = 342$) was achieved by cleavage of amino acids, formamide, and hydroxyl groups. Due to the strong oxidizing capacity of h^+ , P7 underwent a ring cleavage reaction to form P8 ($m/z = 318$), which is further converted to P9 ($m/z = 274$). Similar degradation intermediates have been reported.

The toxicity evaluation software (TEST 4.2.1) based on the

quantitative structure-activity relationship (QSAR) method was used to evaluate the acute toxicity and developmental toxicity of the degradation products [60]. As can be seen from Fig. 12e, the lethal concentration of TC for blackhead minnow 50 (LC50, 96 h) is 0.9 mg L⁻¹, which is significantly lower than that of most degradation intermediates such as P10, P3, and P4, which verifies that the virulence of most degradation products decreases sharply. In addition, as can be seen in Fig. 12f, the photocatalytic reaction system also reduced the developmental toxicity of all products compared to TC (0.89) (except P2, P6, P9). Based on the above facts, the photocatalytic system can significantly reduce and weaken the acute toxicity and developmental toxicity of TC.

3.5. Proposed mechanism

To explore the active radicals that play a role in the photocatalytic reaction, AgNO₃, EDTA-2Na, and N₂ were used as trapping agents to

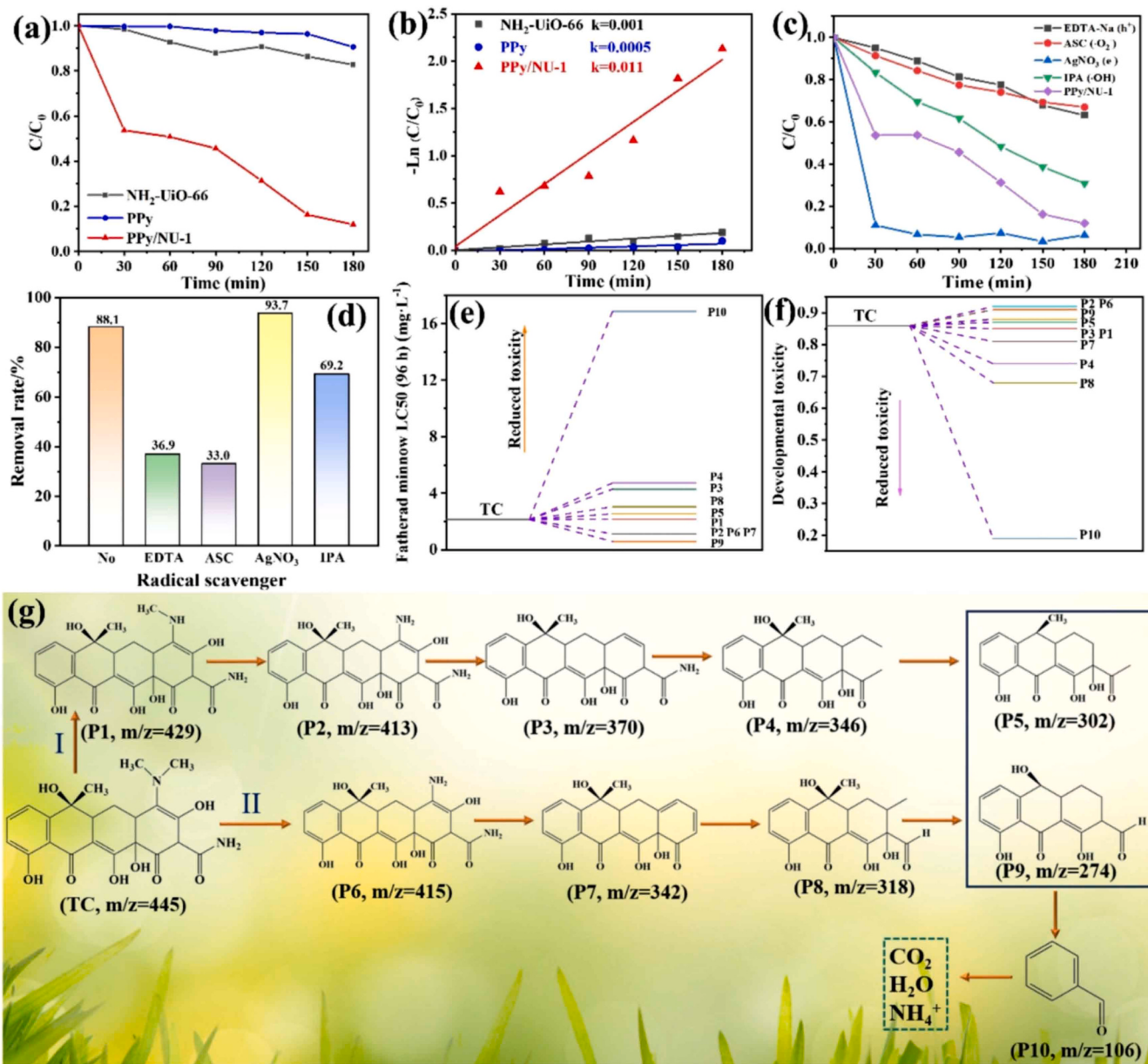


Fig. 12. (a) Photocatalytic degradation of TC over samples under visible light irradiation, (b) the pseudo-first-order kinetics. (c, d) Free radical capture experiments. (e) The acute toxicity, (f) the developmental toxicity of TC and its degradation intermediates, and (g) the proposed photocatalytic-degradation pathways of TC by PPy/NU-1.

study the effects on the reduction of Cr(VI) by PPy/NU-1 [54]. The addition of only AgNO₃ during the reaction inhibits the reaction rate, proving that e^- is the dominant active material (Fig. S3). The inhibition effect was not obvious after the introduction of N₂, indicating that $\bullet\text{O}_2$ was a secondary active species. In addition, the generation of $\bullet\text{O}_2$ and $\bullet\text{OH}$ on the surface of the PPy/NU-1 catalyst was monitored by the NBT method and TA method [65]. The peak value of the NBT- $\bullet\text{O}_2$ adduct gradually decreased with the duration of illumination, while the peak of the TA- $\bullet\text{OH}$ adduct gradually increased with the duration of illumination, which further confirmed the existence of $\bullet\text{O}_2$ and $\bullet\text{OH}$ active species (Fig. 13(a, b)). Finally, ESR technology can further verify the role of $\bullet\text{O}_2$ and $\bullet\text{OH}$. According to the ESR results, the peaks of DMPO- $\bullet\text{O}_2$ and DMPO- $\bullet\text{OH}$ could be detected, which indicated that PPy/NU-1 could generate $\bullet\text{O}_2$ and $\bullet\text{OH}$ under illumination.

To understand the charge distribution state of the PPy/NU-66 photocatalyst, we studied the electronic structures of the original NH₂-UiO-66 and PPy/NU-1 by DFT calculations [47,66,67]. In the NH₂-UiO-66

matrix (Fig. 14a), the amino bonding of PPy to the NH₂-UiO-66 organic ligand is a stable configuration model (Fig. 14b). Therefore, subsequent calculations will be based on this configuration model. The space charge distribution is shown in Fig. 14c, where the yellow area represents the charge accumulation and the blue area represents the charge depletion. It can be seen that there is a significant charge exchange between NH₂-UiO-66 and PPy, which further confirms that charge transfer is achieved near the contact surface, thereby improving the catalytic activity. These results also show that e^- tends to shift from NH₂-UiO-66 to PPy, and an internal electric field forms at the contact interface until the electron diffusion reaches equilibrium. Fig. 14(d-f) shows the calculated total density of states (TDOS) and partial density of states (PDOS) [47, 66]. Compared with the TDOS of NH₂-UiO-66, the highest occupied molecular orbital (HOMO) and the lowest unoccupied molecular orbital (LUMO) were smaller after PPy was added to NH₂-UiO-66 to narrow the band gap, which was consistent with the UV-vis experimental results (Fig. 14d). The Fermi level (E_f) of PPy/NU-1 has also moved to the

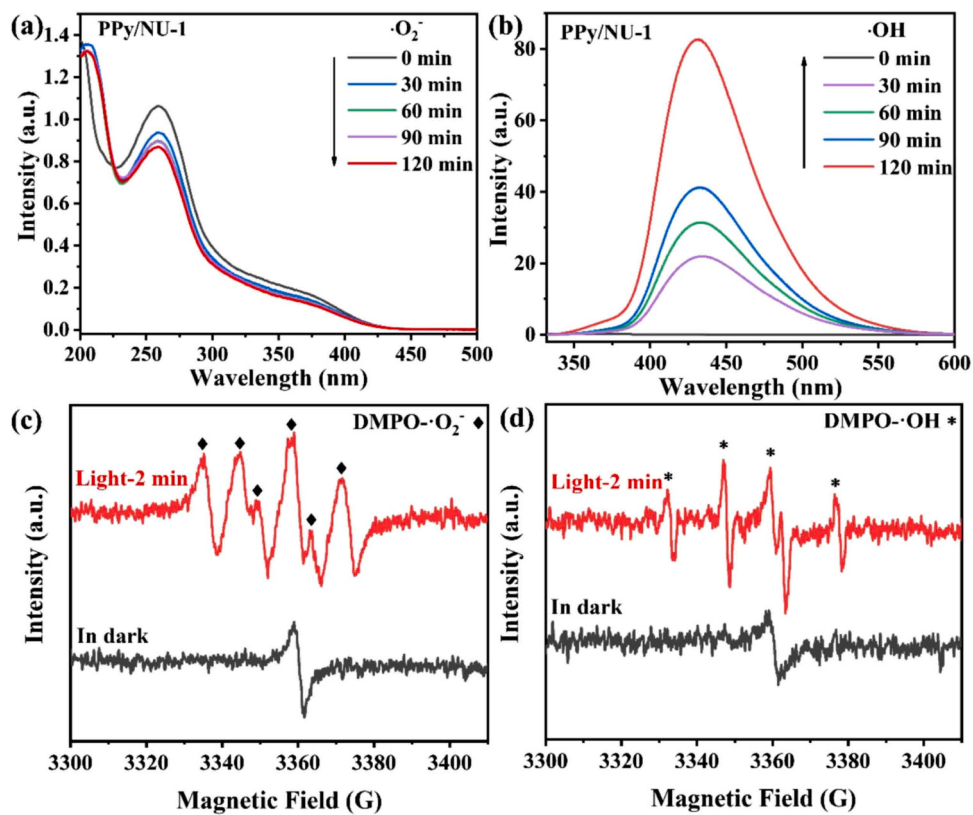


Fig. 13. (a) UV-Vis absorbance spectra of aqueous NBT, (b) Fluorescence spectra of terephthalic acid (TA), (c) DMPO-•O₂⁻, DMPO-•OH over PPy/NU-1.

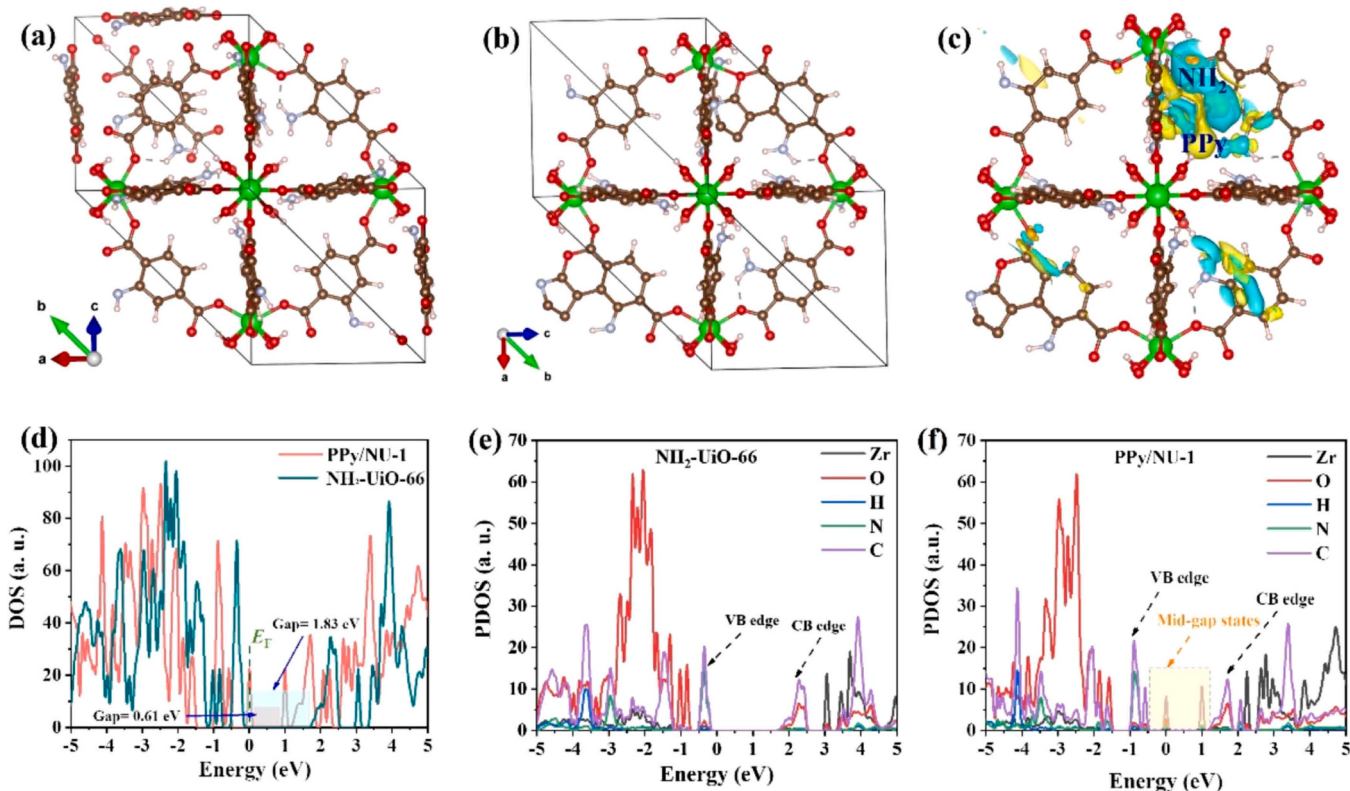
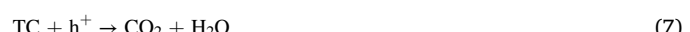


Fig. 14. (a) DFT computational configuration of NH₂-UiO-66. (b) DFT computational configuration of PPy/NU-1. (c) The charge density of PPy/NU-1 with the isovalue of 0.003 a. u., the yellow isosurface depicts the charge accumulation, while the blue one represents charge depletion. (d) TDOS plots for NH₂-UiO-66 and PPy/NU-1. PDOS plots for (e) NH₂-UiO-66 and (f) PPy/NU-1.

bottom of LUMO, indicating that the PPy structure of the composite promotes the number of e^- migration. The PDOS of PPy/NU-1 and NH₂-UiO-66 were further compared, revealing the promotion of e^- migration in the composites. The contribution of PPy in occupying molecular orbitals (formation of mid-gaps states) was found to be the main reason for the narrow band gap of PPy/NU-1 and the downshift of the conduction band to E_f (Fig. 14(e, f)). The results of TDOS were consistent with those of spatial charge distribution PDOS. The above results confirm that the introduction of PPy is conducive to the enrichment of electrons on PPy/NU-1, and creates conditions for the formation of a strong redox process of Z-scheme heterojunction.

Based on the above discussion, the carrier transfer process on the Z scheme heterojunction PPy/NU-1 composite catalyst is proposed. As shown in Fig. 15, NU-66 is an n-type semiconductor with a Fermi level (E_f) close to the LUMO position; PPy is a p-type semiconductor with E_f close to the HUMO position. The close contact between NU-66 and PPy causes the charge to be redistributed to equilibrate E_f . The e^- diffuses from NU-66 to PPy, so that the negative charge accumulates in the PPy region; the h^+ diffuses from PPy to NU-66, allowing a positive charge to accumulate in the NU-66 region. When the E_f is equilibrium, a built-in electric field (IEF) is formed inside the Z-scheme heterojunction directed in the direction of PPy by NU-66. Under illumination, the carriers induced by NU-66 and PPy were subjected to the dual effects of the Z-scheme internal electric field and potential difference. Furthermore, the electron of LUMO on PPy can convert O₂ to •O₂ (O₂/•O₂, -0.33 V vs. NHE) [68]. The HUMO size of NU-66 is positive to the redox potential of OH/•OH (1.99 V vs. NHE), so h^+ converts OH⁻ to •OH.

According to the above experimental results, the electron-hole transfer path of the Z-scheme mechanism could be summarized. First, NH₂-UiO-66 and PPy were produced e^- - h^+ pairs. Since the interface between NH₂-UiO-66 and PPy forms an internal electric field (IEF), a Z-scheme heterojunction is formed under the action of E_f to redistribute the charge to equilibrate E_f [69–71]. In addition, since the Z-scheme heterojunction also exhibits extremely positive VB potential energy and extremely negative CB potential energy, this increases to production of active species. Therefore, the PPy/NU-1 exhibits excellent photoreduction catalytic performance for Cr(VI) reduction and TC degradation. Fig. 15 shows the potential photocatalytic mechanism of the PPy/NU-1, which can be described by the following equation [35,72,73]:



4. Conclusion

In conclusion, PPy/NH₂-UiO-66 Z-scheme heterojunction photocatalysts were successfully synthesized by ball milling. Due to its ultrahigh redox potential, the PPy/NH₂-UiO-66 was easy to generate active substances, thereby enhancing its photocatalytic performance. Through the experiment of modulating a series of environmental factors (such as pH, coexistence cation, anion, organic matter, etc.) and cycling experiments, it is shown that PPy/NU-1 has been widely used and shows good stability. The Cr(VI) removal from industrial electroplating wastewater can reach as high as 99% by photocatalysis of PPy/NU-1. The photocatalytic degradation of TC was also studied in detail, and the toxicity analysis of the intermediate products in the reaction path was carried out, which showed that the excellent photocatalytic degradation of TC could also reduce the toxicity of TC. In addition, the Z-scheme mechanism was reasonably demonstrated by ESR techniques, NBT and TA transformation, and active species capture experiments. The difference between the density of states and the charge density calculated by DFT reveals the formation of heterojunctions, band bending, and internal electric fields at the interface. This work will inspire the development of efficient and stable photocatalytic materials based on NH₂-UiO-66 materials.

CRediT authorship contribution statement

Qian Jianying: Methodology. **Zhou Qi:** Data curation. **Huang Lin-
gye:** Formal analysis. **Zheng Sirui:** Formal analysis. **Li Qiang:** Data
curation. **Hao Derck:** Writing – review & editing. **Deng Hao:** Formal
analysis. **Li Shuangjun:** Data curation. **Zheng Shuzhen:** Investigation.
Ma Wanggang: Resources. **Du Hao:** Writing – review & editing. **Yang
Guoxiang:** Writing – original draft, Writing – review & editing. **Wang
Qi:** Funding acquisition, Supervision.

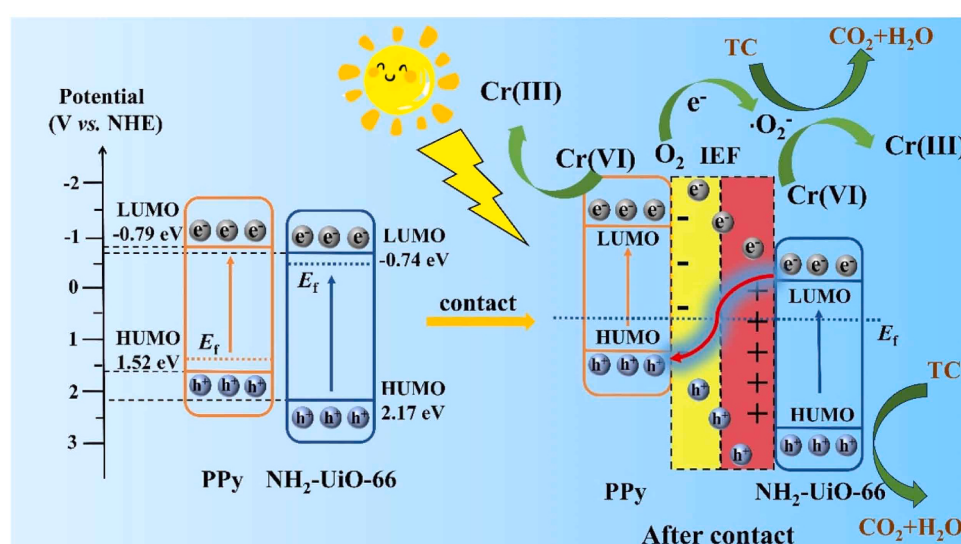


Fig. 15. Description of the potential photocatalytic mechanism of PPy/NU-1.

Declaration of Competing Interest

The authors state that they have no known competing economic interests or personal relationships that could affect the work reported in this paper.

Data availability

Data will be made available on request.

Acknowledgments

This work was supported by the National Natural Science Foundation of China (22276168) and Zhejiang Provincial Natural Science Foundation of China (LQ24B070001). The financial support from Zhejiang Education Department of China (Y202352478) and Basic Research Expenses of Zhejiang Gongshang University (QRK23025) were also thanked. The authors would like to thank the XRD, SEM, TEM, and XPS tests by the Shiyanjia lab (www.shiyanjia.com).

Appendix A. Supporting information

Supplementary data associated with this article can be found in the online version at [doi:10.1016/j.apcatb.2023.123669](https://doi.org/10.1016/j.apcatb.2023.123669).

References

- [1] Q. Wang, L. Wang, S. Zheng, M. Tan, L. Yang, Y. Fu, Q. Li, H. Du, G. Yang, The strong interaction and confinement effect of Ag@NH₂-MIL-88B for improving the conversion and durability of photocatalytic Cr(VI) reduction in the presence of a hole scavenger, *J. Hazard. Mater.* 451 (2023), 131149.
- [2] H. Du, X. Ma, N. Li, L. Yang, Y. Guo, Q. Li, Q. Wang, Exceptional visible-light photoelectrocatalytic activity of dual Z-scheme Bi@BiO_{1-x}Bi_xO₃/C₃N₄ heterojunction for simultaneous remediation of Cr(VI) and phenol, *J. Colloid Interf. Sci.* 640 (2023) 132–143.
- [3] F. Chen, Y. Zhang, H. Huang, Layered photocatalytic nanomaterials for environmental applications, *Chin. Chem. Lett.* 34 (2023) 107523.
- [4] H. Guo, C.-G. Niu, L. Zhang, X.-J. Wen, C. Liang, X.-G. Zhang, D.-L. Guan, N. Tang, G.-M. Zeng, Construction of direct Z-scheme AgI/Bi₂Sn₂O₇ nanojunction system with enhanced photocatalytic activity: accelerated interfacial charge transfer induced efficient Cr(VI) reduction, tetracycline degradation and Escherichia coli inactivation, *ACS Sustain. Chem. Eng.* 6 (2018) 8003–8018.
- [5] H. Du, N. Li, L. Yang, Q. Li, G. Yang, Q. Wang, Plasmonic Ag modified Ag₃VO₄/AgPMo S-scheme heterojunction photocatalyst for boosted Cr(VI) reduction under visible light: performance and mechanism, *Sep. Purif. Technol.* 304 (2023), 122204.
- [6] Y.-X. Li, Y.-C. Han, C.-C. Wang, Fabrication strategies and Cr(VI) elimination activities of the MOF-derivatives and their composites, *Chem. Eng. J.* 405 (2021), 126648.
- [7] J. Lu, Z. Liu, Z. Wu, W. Liu, C. Yang, Synergistic effects of binary surfactant mixtures in the removal of Cr(VI) from its aqueous solution by foam fractionation, *Sep. Purif. Technol.* 237 (2020), 116346.
- [8] F. Deng, X. Lu, Y. Luo, J. Wang, W. Che, R. Yang, X. Luo, S. Luo, D.D. Dionysiou, Novel visible-light-driven direct Z-scheme CdS/CuInS₂ nanoplates for excellent photocatalytic degradation performance and highly-efficient Cr(VI) reduction, *Chem. Eng. J.* 361 (2019) 1451–1461.
- [9] L. Yang, Y. Fu, F. Sun, M. Deng, C. Zhang, N. Li, D. Hao, Q. Wang, G. Zhuang, Preparation of novel diperylene-cored polyimide photocatalyst with broad-spectra response and high stability, *J. Colloid Interf. Sci.* 639 (2023) 472–483.
- [10] Q. Wang, K. Zhang, S. Zheng, X. Hu, L. Wang, H. Du, D. Hao, G. Yang, An innovative AgI/MIL-100 (Fe) Z-scheme heterojunction for simultaneously enhanced photoreduction of Cr(VI) and antibacterial activity, *Appl. Surf. Sci.* 616 (2023), 156528.
- [11] B.A. Marinho, R.O. Cristóvão, R. Djellabi, J.M. Loureiro, R.A. Boaventura, V. J. Vilar, Photocatalytic reduction of Cr(VI) over TiO₂-coated cellulose acetate monolithic structures using solar light, *Appl. Catal. B: Environ.* 203 (2017) 18–30.
- [12] X. Li, J. Liu, J. Feng, T. Wei, Z. Zhou, J. Ma, Y. Ren, Y. Shen, High-ratio {100} plane-exposed ZnO nanosheets with dual-active centers for simultaneous photocatalytic Cr(VI) reduction and Cr(III) adsorption from water, *J. Hazard. Mater.* 445 (2023), 130400.
- [13] M. Ghorbani, A.R.S. Nazar, M. Farhadian, S. Tangestaninejad, Efficient tetracycline degradation and electricity production in photocatalytic fuel cell based on ZnO nanorod/BiOBr/Uio-66-NH₂ photoanode and Cu₂O/CuO photocathode, *Energy* 272 (2023), 127114.
- [14] S. Zheng, H. Du, L. Yang, M. Tan, N. Li, Y. Fu, D. Hao, Q. Wang, PDINH bridged NH₂-Uio-66(Zr) Z-scheme heterojunction for promoted photocatalytic Cr(VI) reduction and antibacterial activity, *J. Hazard. Mater.* 447 (2023), 130849.
- [15] Q. Li, E. Wang, H. Zhou, Y. Fu, H. Deng, Y. Zheng, B. Xue, H. Du, G. Yang, Q. Wang, Accelerated electron and mass transfer through constructing H₂WO₄/Ti₃C₂/g-C₃N₄ Z-scheme photocatalyst for environmental remediation, *Chemosphere* (2023), 140053.
- [16] X. Li, C. Garlisi, Q. Guan, S. Anwer, K. Al-Ali, G. Palmisano, L. Zheng, A review of material aspects in developing direct Z-scheme photocatalysts, *Mater. Today* 47 (2021) 75–107.
- [17] C. Avci, I. Imaz, A. Carné-Sánchez, J.A. Pariente, N. Tasios, J. Pérez-Carvalj, M. I. Alonso, A. Blanco, M. Dijkstra, C. López, Self-assembly of polyhedral metal-organic framework particles into three-dimensional ordered superstructures, *Nat. Chem.* 10 (2018) 78–84.
- [18] J. Dai, D. Wang, J. Yang, R. Tian, Q. Wang, Y. Li, Construction of imidazole@ defective hierarchical porous Uio-66 and fibrous composites for rapid and nonbuffered catalytic hydrolysis of organophosphorus nerve agents, *J. Colloid Interf. Sci.* 652 (2023) 1156–1169.
- [19] Y. Wang, Q. Yang, F. Yi, R. Lu, Y. Chen, C. Liu, X. Li, C. Wang, H. Yan, NH₂-UiO-66 coated with two-dimensional covalent organic frameworks: high stability and photocatalytic activity, *ACS Appl. Mater. Inter.* 13 (2021) 29916–29925.
- [20] S. Shahabuddin, R. Gaur, N. Mukherjee, P. Chandra, R. Khanam, Conducting polymers-based nanocomposites: Innovative materials for waste water treatment and energy storage, *Mater. Today*: Proc.
- [21] R. Bulakhe, S. Patil, P. Deshmukh, N. Shinde, C. Lokhande, Fabrication and performance of polypyrrole (PPy)/TiO₂ heterojunction for room temperature operated LPG sensor, *Sens. Actuat. B Chem.* 181 (2013) 417–423.
- [22] W. Zhang, X. Song, L. Ling, Z. Wang, X. Hao, G. Guan, Terminal-dependent ion recognition of BiOBr/PPy hybrid film with befitting absorption function for rapidly selective bromine ions removal, *Chem. Eng. J.* 457 (2023), 141213.
- [23] P.H. Dinh, T.-D. Pham, D. Van Thuan, N.T.D. Cam, N.T. Hanh, H. Van, Ha, N.H. A. Thu, H.T. Trang, N.L.M. Tri, CuWO₄ decorated by polypyrrole (PPy) protector/sensitizer for novel photocatalytic and stable water splitting for hydrogen generation, *Int. J. Hydron. Energ.* 45 (2020) 21442–21449.
- [24] Y. Chen, X. Xin, D. Yang, H. Ren, Y. Gao, Z. Zhao, W. Wang, K. An, J. Tan, Z. Jiang, Pyrimidine-modified g-C₃N₄ nanosheets for enhanced photocatalytic H₂ evolution, *Mater. Res. Bull.* 144 (2021), 111498.
- [25] V.-D. Dao, N.T.P. Le Chi, D. Van Thuan, T.-D. Pham, D.-T. Tran, M.P. Nguyen, P. Thao, M.V. Nguyen, N.T.D. Cam, N.M. Tuong, Superior stability and photocatalytic activity of Ta₃N₅ sensitized/protected by conducting polymers for water splitting, *J. Alloy. Compd.* 775 (2019) 942–949.
- [26] S.M. Amorim, G. Steffen, J.M. de S Junior, C.Z. Brusamarello, A.P. Romio, M. D. Domenico, Synthesis, characterization, and application of polypyrrole/TiO₂ composites in photocatalytic processes: a review, *Polym. Polym. Compos.* 29 (2021) 1055–1074.
- [27] Y. Liang, X. Wang, W. An, Y. Li, J. Hu, W. Cui, A g-C₃N₄@ppy-rGO 3D structure hydrogel for efficient photocatalysis, *Appl. Surf. Sci.* 466 (2019) 666–672.
- [28] N.T.T. Truc, D.T. Tran, N.T. Hanh, T.-D. Pham, Novel visible light-driven Nb-doped Ta₃N₅ sensitized/protected by PPy for efficient overall water splitting, *Int. J. Hydron. Energ.* 43 (2018) 15898–15906.
- [29] Y. Li, S. Yan, X. Jia, J. Wu, J. Yang, C. Zhao, S. Wang, H. Song, X. Yang, Uncovering the origin of full-spectrum visible-light-responsive polypyrrole supramolecular photocatalysts, *Appl. Catal. B: Environ.* 287 (2021), 119926.
- [30] X. Wei, C.-C. Wang, Y. Li, P. Wang, Q. Wei, The Z-scheme NH₂-UiO-66/PTCDA composite for enhanced photocatalytic Cr(VI) reduction under low-power LED visible light, *Chemosphere* 280 (2021), 130734.
- [31] Q. Wang, L. Zheng, Y. Chen, J. Fan, H. Huang, B. Su, Synthesis and characterization of novel PPy/Bi₂O₃CO₃ composite with improved photocatalytic activity for degradation of Rhodamine-B, *J. Alloy. Compd.* 637 (2015) 127–132.
- [32] H. Molavi, F.A. Joukani, A. Shojaei, Ethylenediamine grafting to functionalized NH₂-UiO-66 using green aza-michael addition reaction to improve CO₂/CH₄ adsorption selectivity, *Ind. Eng. Chem. Res.* 57 (2018) 7030–7039.
- [33] S. Li, H.-Y. Zeng, J. Xiong, S. Xu, Polypyrrole decorated ZnTi hydroalcite with enhanced adsorption and Cr(VI) photoreduction activity under visible-light, *Adv. Powder Technol.* 32 (2021) 3090–3100.
- [34] J. Ren, S. Lv, S. Wang, M. Bao, X. Zhang, Y. Gao, Y. Liu, Z. Zhang, L. Zeng, J. Ke, Construction of efficient g-C₃N₄/NH₂-UiO-66(Zr) heterojunction photocatalysts for wastewater purification, *Sep. Purif. Technol.* 274 (2021), 118973.
- [35] Z. Lin, Y. Wu, X. Jin, D. Liang, Y. Jin, S. Huang, Z. Wang, H. Liu, P. Chen, W. Lv, Facile synthesis of direct Z-scheme UiO-66-NH₂/PhC₆Cu heterojunction with ultrahigh redox potential for enhanced photocatalytic Cr(VI) reduction and NOR degradation, *J. Hazard. Mater.* 443 (2023), 130195.
- [36] Q. Hu, Y. Chen, M. Li, Y. Zhang, B. Wang, Y. Zhao, J. Xia, S. Yin, H. Li, Construction of NH₂-UiO-66/BiOBr composites with boosted photocatalytic activity for the removal of contaminants, *Colloids Surf. A* 579 (2019), 123625.
- [37] D. Liu, Y. Li, C. Liu, Y. Zhou, Facile preparation of UiO-66@PPy nanostructures for rapid and efficient adsorption of fluoride: Adsorption characteristics and mechanisms, *Chemosphere* 289 (2022), 133164.
- [38] N. Ahmad, S. Sultan, S. Sabir, M.Z. Khan, Exploring the visible light driven photocatalysis by reduced graphene oxide supported Ppy/CdS nanocomposites for the degradation of organic pollutants, *J. Photoch. Photobio. A* 386 (2020), 112129.
- [39] J. Chen, H. You, L. Xu, T. Li, X. Jiang, C.M. Li, Facile synthesis of a two-tier hierarchical structured superhydrophobic-superoleophilic melamine sponge for rapid and efficient oil/water separation, *J. Colloid Interf. Sci.* 506 (2017) 659–668.
- [40] F. Zhou, Y. Li, S. Wang, X. Wu, J. Peng, F. Wang, L. Wang, J. Mao, Turning waste into valuables: In situ deposition of polypyrrole on the obsolete mask for Cr(VI) removal and desalination, *Sep. Purif. Technol.* 306 (2023), 122643.

- [41] M.B. Hussain, R. Mehmood, U. Azhar, J. Wang, L. Song, BiOCl-coated UiO-66-NH₂ metal-organic framework nanoparticles for visible-light photocatalytic Cr(VI) reduction, *ACS Appl. Nano Mater.* 4 (2021) 4037–4047.
- [42] J. Liu, X. Huang, L. Jia, L. Liu, Q. Nie, Z. Tan, H. Yu, Microwave-assisted rapid substitution of Ti for Zr to produce bimetallic (Zr/Ti) UiO-66-NH₂ with congeneric “shell-core” structure for enhancing photocatalytic removal of nitric oxide, *Small* (2023), 2207198.
- [43] Q. Su, J. Li, B. Wang, Y. Li, Direct Z-scheme Bi₂MoO₆/UiO-66-NH₂ heterojunctions for enhanced photocatalytic degradation of ofloxacin and ciprofloxacin under visible light, *Appl. Catal. B: Environ.* 318 (2022), 121820.
- [44] J. Guo, L. Wang, Y. Tu, H. Muhammad, X. Fan, G. Cao, M. Laipan, Polypyrrole modified bentonite nanocomposite and its application in high-efficiency removal of Cr(VI), *J. Environ. Chem. Eng.* 9 (2021), 106631.
- [45] Z. Ye, S. Feng, W. Wu, Y. Zhou, Y. Wang, X. Dai, X. Cao, Synthesis of double MOFs composite material for visible light photocatalytic degradation of tetracycline, *Solid State Sci.* 127 (2022), 106842.
- [46] S. Xiao, Y. Guan, H. Shang, H. Li, Z. Tian, S. Liu, W. Chen, J. Yang, An S-scheme NH₂-UiO-66/SiC photocatalyst via microwave synthesis with improved CO₂ reduction activity, *J. CO₂ Util.* 55 (2022), 101806.
- [47] S. Li, H. Shang, Y. Tao, P. Li, H. Pan, Q. Wang, S. Zhang, H. Jia, H. Zhang, J. Cao, B. Zhang, R. Zhang, G. Li, Y. Zhang, D. Zhang, H. Li, Hydroxyl radical-mediated efficient photoelectrocatalytic NO oxidation with simultaneous nitrate storage using a flow photoanode reactor, *Angew. Chem. Int. Ed.* 62 (2023), e202305538.
- [48] G. Yang, L. Wang, S. Zheng, H. Wu, D. Hao, Q. Li, H. Du, H. Yamashita, Q. Wang, Novel dual Z-scheme Ag-bridged AgI/FeVO₄-C₃N₄ plasmonic heterojunction: a study on the performance and mechanism of photocatalytic reduction of Cr(VI), *J. Environ. Chem. Eng.* 11 (2023), 110071.
- [49] L. Wang, K. Zhang, J. Qian, M. Qiu, N. Li, H. Du, X. Hu, Y. Fu, M. Tan, D. Hao, Q. Wang, S-scheme MOF-on-MOF heterojunctions for enhanced photo-Fenton Cr (VI) reduction and antibacterial effects, *Chemosphere* 344 (2023) 140277.
- [50] C.-C. Wang, X. Ren, P. Wang, C. Chang, The state of the art review on photocatalytic Cr(VI) reduction over MOFs-based photocatalysts: From batch experiment to continuous operation, *Chemosphere* 303 (2022), 134949.
- [51] G. Corro, N. Sánchez, U. Pal, S. Cebada, J.L.G. Fierro, Solar-irradiation driven biodiesel production using Cr/SiO₂ photocatalyst exploiting cooperative interaction between Cr⁶⁺ and Cr³⁺ moieties, *Appl. Catal. B: Environ.* 203 (2017) 43–52.
- [52] B. Mbali, M. Mahlambi, C.J. Ngila, R. Moutloali, Polysulfone ultrafiltration membranes modified with carbon-coated alumina supported NiTiO₂ nanoparticles for water treatment: synthesis, characterization and application, *J. Membr. Sci. Res* 5 (2019) 222–232.
- [53] Q. Cen, Q. Gao, C. Zhang, Y. Liu, Q. Wang, Photocatalytic reduction of Cr(VI) by iron tungstosilicate under visible light, *J. Colloid Interface Sci.* 562 (2020) 12–20.
- [54] M. Deng, J. Guo, X. Ma, Y. Fu, H. Du, D. Hao, Q. Wang, Enhanced photocatalytic Cr (VI) reduction performance by novel PDI/COFs composite, *Sep. Purif. Technol.* 326 (2023), 124786.
- [55] Y. Liu, F. Gao, S. Liu, H. Liu, M. Fang, X. Tan, Visible and infrared light photocatalysis of Cr(VI) by CdTe nanoparticles, *Appl. Surf. Sci.* 615 (2023), 156399.
- [56] S. Luo, F. Qin, Ya Ming, H. Zhao, Y. Liu, R. Chen, Fabrication uniform hollow Bi₂S₃ nanospheres via Kirkendall effect for photocatalytic reduction of Cr(VI) in electroplating industry wastewater, *J. Hazard. Mater.* 340 (2017) 253–262.
- [57] R. He, Z. Wang, F. Deng, X. Li, Y. Peng, Y. Deng, J. Zou, X. Luo, X. Liu, Tunable Bi-bridge S-scheme Bi₂S₃/BiOBr heterojunction with oxygen vacancy and SPR effect for efficient photocatalytic reduction of Cr(VI) and industrial electroplating wastewater treatment, *Sep. Purif. Technol.* 311 (2023), 123176.
- [58] M.D. Goudarzi, N. Khosroshahi, A. Hamlehdar, V. Safarifard, Construction of S-scheme heterojunction via incorporating g-C₃N₄ into Ce-based MOFs for promotion of charge-transfer in photocatalytic Cr(VI) detoxification, *J. Environ. Chem. Eng.* 11 (2023), 110169.
- [59] C. Liu, H. Dai, C. Tan, Q. Pan, F. Hu, X. Peng, Photo-Fenton degradation of tetracycline over Z-scheme Fe-g-C₃N₄/Bi₂WO₆ heterojunctions: mechanism insight, degradation pathways and DFT calculation, *Appl. Catal. B: Environ.* 310 (2022), 121326.
- [60] J. Li, Z. Zhao, Z. Li, H. Yang, S. Yue, Y. Tang, Q. Wang, Construction of immobilized films photocatalysts with CdS clusters decorated by metal Cd and BiOCl for photocatalytic degradation of tetracycline antibiotics, *Chin. Chem. Lett.* 33 (2022) 3705–3708.
- [61] Y. Zhou, Q. Li, J. Zhang, M. Xiang, Y. Zhou, Z. Chen, Y. Chen, T. Yao, Broad spectrum driven Y doped BiO_{2-x} for enhanced degradation of tetracycline: Synergy between singlet oxygen and free radicals, *Appl. Surf. Sci.* 607 (2023), 154957.
- [62] T. Song, X. Meng, H. Wang, C. Zhang, M. Ge, Visible-LED-light-driven photocatalytic activation of peroxydisulfate by magnetic ZnFe₂O₄/Ag nanocomposite for efficient tetracycline degradation, *Sep. Purif. Technol.* 297 (2022), 121474.
- [63] X. Meng, Q. He, T. Song, M. Ge, Z. He, C. Guo, Activation of peroxydisulfate by magnetically separable rGO/MnFe₂O₄ toward oxidation of tetracycline: efficiency, mechanism and degradation pathways, *Sep. Purif. Technol.* 282 (2022), 120137.
- [64] C. Liu, S. Mao, H. Wang, Y. Wu, F. Wang, M. Xia, Q. Chen, Peroxymonosulfate-assisted for facilitating photocatalytic degradation performance of 2D/2D WO₃/BiOBr S-scheme heterojunction, *Chem. Eng. J.* 430 (2022), 132806.
- [65] Y. Fu, Y. Xu, Y. Mao, M. Tan, Q. He, H. Mao, H. Du, D. Hao, Q. Wang, Multi-functional Ag/Ag₃PO₄/AgPMo with S-scheme heterojunction for boosted photocatalytic performance, *Sep. Purif. Technol.* 317 (2023), 123922.
- [66] G. Wang, C.T. He, R. Huang, J. Mao, D. Wang, Y. Li, Photoinduction of Cu single atoms decorated on UiO-66-NH₂ for enhanced photocatalytic reduction of CO₂ to liquid fuels, *J. Am. Chem. Soc.* 142 (2020) 19339–19345.
- [67] S. Kaviani, D.A. Tayurskii, O.V. Nedopekin, I. Piyanzina, DFT-based modeling of polypyrole/B₁₂N₁₂ nanocomposite for the photocatalytic applications, *J. Phys. Chem. Solids* 170 (2022), 110949.
- [68] B. Xue, Q. Li, L. Wang, M. Deng, H. Zhou, N. Li, M. Tan, D. Hao, H. Du, Q. Wang, Ferric-ellaglate complex: a promising multifunctional photocatalyst, *Chemosphere* 332 (2023), 138829.
- [69] R. Jiang, L. Mao, Y. Zhao, J. Zhang, E.B. Chubenko, V. Bondarenko, Y. Sui, X. Gu, X. Cai, 1D/2D CeO₂/ZnIn₂S₄ Z-scheme heterojunction photocatalysts for efficient H₂ evolution under visible light, *Sci. China Mater.* 66 (2023) 139–149.
- [70] P.J. Mafa, M.E. Malefane, F. Opoku, B.B. Mamba, A.T. Kuvarega, Visible light responsive MoS₂/Ag@WO₃/EG photoanode with highly stable Z-scheme induced circular electron motion pioneered by exfoliated graphite for bisphenol a photodegradation, *Chem. Eng. J.* 464 (2023), 142462.
- [71] Q. Wu, L. Tan, X. Liu, Z. Li, Y. Zhang, Y. Zheng, Y. Liang, Z. Cui, S. Zhu, S. Wu, The enhanced near-infrared photocatalytic and photothermal effects of MXene-based heterojunction for rapid bacteria-killing, *Appl. Catal. B: Environ.* 297 (2021), 120500.
- [72] Y. Zhang, P. Tan, L. Yang, S. Zhang, B. Zhou, X. Zhang, H. Huang, J. Pan, Mannitol-assisted Fe-O clusters@ZIF-L for Cr(VI) photocatalytic reduction under neutral conditions inspired by Fe-based MOFs photocatalysts, *Sep. Purif. Technol.* 320 (2023), 124174.
- [73] D. Gu, Y. Liu, X. Li, H. Zhu, Y. Cui, W. Yang, J. Hao, Porphyrin-based metal-organic frameworks loaded with Ag nanoparticles and their nanofibrous filters for the photocatalytic reduction of Cr(VI), *Appl. Surf. Sci.* 614 (2023), 156192.